

¹ RESEARCH

² **Modelling the cell-type specific mesoscale murine connectome with
3 anterograde tracing experiments**

⁴ **Samson Koelle**^{1,2}, **Jennifer D Whitesell**¹, **Karla E Hirokawa**¹, **Hongkui Zeng**¹, **Marina Meila**², **Julie A Harris**¹, **Stefan
5 Mihalas**¹

⁶ ¹ Allen Institute for Brain Science, Seattle, WA, USA

⁷ ²Department of Statistics, University of Washington, Seattle, WA, USA

⁸ **Keywords:** [Connectivity, Cell-type, Mouse]

ABSTRACT

⁹ The Allen Mouse Brain Connectivity Atlas consists of anterograde tracing experiments targeting
¹⁰ diverse structures and classes of projecting neurons. Beyond regional anterograde tracing done in
¹¹ C57BL/6 wild type mice, a large fraction of experiments are performed using transgenic Cre-lines.
¹² This allows access to cell-class specific whole brain connectivity information, with class defined by
¹³ the transgenic lines. However, even though the number of experiments is large, it does not come close
¹⁴ to covering all existing cell classes in every area where they exist. Here, we study how much we can fill
¹⁵ in these gaps and construct a voxel-based connectivity matrix given the observations that nearby
¹⁶ voxels have similar connections when they are in the same area, that connections can change
¹⁷ dramatically at area boundaries, and that particular cell classes can have similar connections, but that
¹⁸ this similarity is region-dependent.

¹⁹ This paper describes the conversion of the Cre-line tracer experiments into class-specific
²⁰ connectivity matrices representing the connection strengths between source and target structures.

21 We introduce and validate a novel statistical model for creation of connectivity matrices. We expand a
22 Nadaraya-Watson kernel learning method which we previously used to fill in spatial gaps, to also fill in
23 a gaps in cell class connectivity information. To do this, we construct a "cell-class space" and combine
24 smoothing in 3D space as well as in this abstract space to share information between similar neuron
25 classes. Using this method we construct a set of connectivity matrices using multiple levels of
26 resolution at which discontinuities in connectivity are assumed. We show that the connectivities
27 obtained from this model display expected cell-type and structure specific connectivities. Inspired by
28 how this complexity arises from a relatively parsimonious set of genetic information during
29 development, we also show that the wild type connectivity matrix can be factored using a sparse set of
30 factors, and analyze the informativeness of this underlying latent structure.

AUTHOR SUMMARY

31 Large-scale studies have described the connections between areas in multiple mammalian models in
32 ever expanding detail. Standard connectivity studies focus on the connection strength between areas.
33 However, when describing functions at a local circuit level, there is an increasing focus on cell types.
34 We have recently described the importance of connection types in the cortico-thalamic system, which
35 allows an unsupervised discovery of its hierarchical organization. In this study we focus on adding a
36 dimension of connection type for a brain-wide mesoscopic connectivity model. Even with our
37 relatively massive dataset, the data in the cell type direction for connectivity is quite sparse, and we
38 had to develop methods to more reliably extrapolate in such directions, and to estimate when such
39 extrapolations are impossible. This allows us to fill in such a connection type specific inter-areal
40 connectivity matrix to the extent our data allows. While analyzing this complex connectivity, we
41 observed that it can be described via a small set of factors. While not complete, this connectivity
42 matrix represents a large leap forward in mouse mesoscale connectivity models.

1 INTRODUCTION

43 The mammalian nervous system enables an extraordinary range of natural behaviors, and has
44 inspired much of modern artificial intelligence. Neural connections from one region to another form
45 the architecture underlying this capability. These connectivities vary by neuron type, as well as source
46 cell body location and target axonal projection structures. Thus, characterization of the relationship
47 between neuron type and source and target structure is important for understanding the overall
48 nervous system.

49 Viral tracing experiments - in which a viral vector expressing GFP is transduced into neural cells
50 through stereotaxic injection - are a useful tool for mapping these connections on the mesoscale (???).
51 The GFP protein moves into the axon of the projecting neurons. The long range connections between
52 different areas are generally formed by axons which travel from one region to another. Two-photon
53 tomography imaging can be used to determine the location and strength of the fluorescent signals in
54 two-dimensional slices. These locations can then be mapped back into three-dimensional space. The
55 signal is integrated over area into cubic voxels.

56 Several statistical models for the conversion of such experiment-specific signals into generalized
57 estimates of connectivity strength have been proposed (????). Of these, ? and ? model **regionalized**
58 **connectivities**, which are voxel connectivities integrated by region. The value of these models is that
59 they provide some improvement over simply averaging the projection signals of injections in a given
60 region. However, these previous works only model connectivities observed in wild type mice in which
61 all neuron types were labeled, and so are poorly suited for extension to tracing experiments that
62 induce cell-type specific fluorescence (?). In particular, GFP expression is induced by
63 Cre-recombinase in cell-types specified by transgenic strain. Thus, this paper introduces a **cell**
64 **class**-specific statistical model to deal with the diverse set of **Cre-lines** described in ?, and expands
65 this model to the entire mouse brain. In cortex a large number of transgenic lines were chosen for
66 their laminar specific expression.

67 Our model is a to-our-knowledge novel estimator that takes into account both the spatial position
68 of the labelled source, as well as the categorical cell class. Like the previously state-of-the-art model in
69 ?, this model predicts regionalized connectivity as an average over positions within the structure, with

70 nearby experiments given more weight. However, our model weighs class-specific behavior in a
71 particular structure against spatial position, so a nearby experiment targeting a similar cell class
72 would be relatively up-weighted, while a nearby experiment targeting a dissimilar class would be
73 down-weighted. This model outperforms the model of ? based on their ability to predict held-out
74 experiments in leave-one-out cross-validation. We establish a lower-limit of detection, and then use
75 the trained model to estimate overall connectivity matrices for each assayed cell class.

76 The resulting cell-type specific connectivity is a directed weighted multigraph which can be
77 represented as a tensor with missing values. We do not attempt an exhaustive analysis of this data, but
78 do manually verify several cell-type specific connectivity patterns found elsewhere in the literature,
79 and show that these cell-type specific signals are behaving in expected ways. Finally, we decompose
80 the wild type connectivity matrix into factors representing archetypal connectivity patterns using
81 non-negative matrix factorization. These components are themselves novel and of some independent
82 interest since they allow approximation of the regionalized connectivity using a small set of latent
83 components. Such components can provide a link to the genetic origin of the regionalized
84 connectivity.

85 Section 2 gives information on the data and statistical methodology, and Section 3 presents our
86 results. These include connectivities, assessments of model fit, and subsequent analyses. Additional
87 information on our dataset, methods, and results are given in Supplemental Sections 5, ??, and ??,
88 respectively.

2 METHODS

We create and analyze cell class-specific connectivity matrices using models trained on murine brain viral tracing experiments. This section describes the data used to generate the model, the model itself, the evaluation of the model, and the use of the model in creation of the connectivity matrices. It also includes background on the non-negative matrix factorization method used for decomposing the wild type connectivity matrix into latent structures. Additional information about our data and methods are given in Supplemental Sections 5 and ??, respectively.

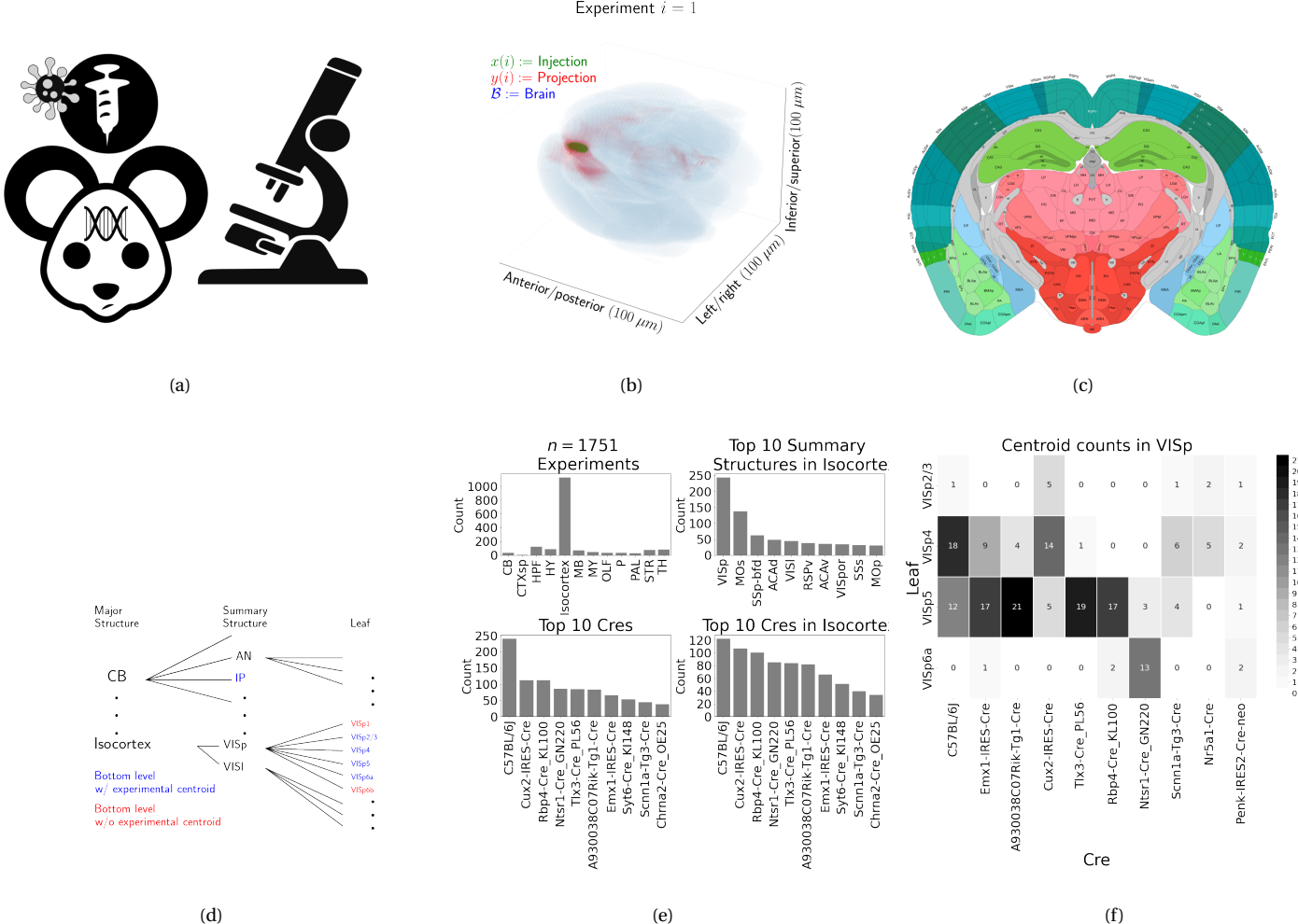


Figure 1: Experimental setting. 1a For each experiment, a Cre-dependent GFP-expressing transgene cassette is transduced by stereotaxic injection into a Cre-driver mouse, followed by serial two-photon tomography imaging. 1b An example of the segmentation of projection (targets) and injection (source) for a single experiment. Within each brain (blue), injection (green) and projection (red) areas are determined via histological analysis and alignment to the Allen Common Coordinate Framework (CCF). 1c Brain region parcellations within a coronal plane of CCFv3. 1d Explanation of nested structural ontology highlighting various levels of CCFv3 structure ontology. Lowest-level (leaf) structures are colored in blue, and structures without an injection centroid are colored in red. 1e Abundances of tracer experiments by Cre line and region of injection. 1f Co-occurrence of layer-specific centroids and Cre lines within VISp.

95 **Data**

96 Our dataset \mathcal{D} consists of $n = 1751$ publicly available murine brain viral tracing experiments from the
 97 Allen Mouse Brain Connectivity Atlas. Figure 1a summarizes the multistage experimental process
 98 used to generate this dataset. In each experiment, a mouse is injected with AAV encoding GFP into a
 99 single location in the brain. For cell type-specific labeling, we used a double-inverted floxed (Cre
 100 inducible) AAV in a Cre driver mouse, producing fluorescence that depends on Cre expression in
 101 infected cells. Cre driver mice are engineered to express Cre under the control of a specific and single
 102 gene promoter. This single gene promoter-mediated expression of Cre in some rare cases corresponds
 103 to a very specific transcriptomic cell-type, but more frequently it corresponds to a combination of fine
 104 level transcriptomic cell-types that represent broader cell classes. For example, we include
 105 experiments from Cre driver lines that selectively label cell classes located in distinct cortical layers or
 106 other nuclei across the whole brain. In wild type mice injected with non-Cre-dependent viruses,
 107 fluorescence is induced in all infected cells in the region (not just those expressing Cre), and so the full
 108 set of projection target areas are visualized from the given injected brain region. We therefore use the
 109 term "cell class" here to refer to all neurons expressing Cre in a specific Cre driver mouse line.

110 For each experiment, the fluorescent signal imaged after injection is aligned into the Allen
 111 Common Coordinate Framework (CCF) v3, a three-dimensional average template brain that is fully
 112 annotated with regional parcellations ?. The informatics data processing pipeline including whole
 113 brain imaging and registration procedures (described in detail in ??) produces quantitative metrics
 114 of fluorescence discretized at the $100 \mu\text{m}$ voxel level. Given an experiment, this image is histologically
 115 segmented into *injection* and *projection* areas corresponding to areas containing somas, dendrites
 116 and axons or exclusively axons of the transfected neurons. An example of a single experiment
 117 rendered in 3D is given in Figure 1b. Given an experiment i , we represent injections and projections
 118 as maps $x(i), y(i) : \mathcal{B} \rightarrow \mathbb{R}_{\geq 0}$, where $\mathcal{B} \subset [1 : 132] \times [1 : 80] \times [1 : 104]$ corresponds to the subset of the
 119 $(1.32 \times 0.8 \times 1.04)$ cm rectangular space occupied by the standard mouse brain. We also calculate
 120 injection centroids $c(i) \in \mathbb{R}^3$ and regionalized projections $y_{\mathcal{T}}(i) \in \mathbb{R}^T$ given by the sum of $y(i)$ in each
 121 region. A detailed mathematical description of these steps, including data quality control, is given in
 122 Supplemental Section ??.

123 Our goal is the estimation of **regionalized connectivity** from one region to another. A visual
124 depiction of this region parcellation for a two-dimensional slice of the brain is given in Figure 1c. All
125 structures annotated in the CCF belong to a hierarchically ordered ontology, with different areas of the
126 brain are parcellated to differing finer depths within a hierarchical tree. We denote the main levels of
127 interest as Major Structures, Summary Structures, and Leaves. As indicated in Figure 1d, the dataset
128 used to generate the connectivity model reported in this paper contains certain combinations of
129 region and cell class frequently, and others not at all. A summary of the most frequently assayed cell
130 classes and structures is given in Figures 1e and 1f. Since users of the connectivity matrices may be
131 interested in particular combinations, or interested in the amount of data used to generate a
132 particular connectivity estimate, we present this information about all experiments in Supplemental
133 Section 5.

134 ***Modeling Regionalized Connectivity***

As a continuous function, cell-class specific connectivity maps $f : \mathcal{V} \times \mathbb{R}^3 \times \mathbb{R}^3 \rightarrow \mathbb{R}_{\geq 0}$, giving the directed connection of a particular cell class from one position in the brain to another. In contrast to ?, which only uses wild type C57BL/6J mice, our dataset has experiments from $V = 114$ different Cre-lines $\mathcal{V} := \{v\}$. As in ?, we ultimately estimate an integrated regionalized connectivity defined with respect to a set of $S = 564$ source regions $\mathcal{S} := \{s\}$ and $T = 1123$ target regions $\mathcal{T} := \{t\}$, of which $1123 - 564 = 559$ are contralateral. That is, we define

$$\text{regionalized connectivity strength } \mathcal{C} : \mathcal{V} \times \mathcal{S} \times \mathcal{T} \rightarrow \mathbb{R}_{\geq 0} \text{ with } \mathcal{C}(v, s, t) = \sum_{l_j \in s} \sum_{l_{j'} \in t} f(v, l_j, l_{j'}),$$

$$\text{normalized regionalized connectivity strength } \mathcal{C}^N : \mathcal{V} \times \mathcal{S} \times \mathcal{T} \rightarrow \mathbb{R}_{\geq 0} \text{ with } \mathcal{C}^N(v, s, t) = \frac{1}{|s|} \mathcal{C}(v, s, t),$$

$$\text{normalized regionalized projection density } \mathcal{C}^D : \mathcal{V} \times \mathcal{S} \times \mathcal{T} \rightarrow \mathbb{R}_{\geq 0} \text{ with } \mathcal{C}^D(v, s, t) = \frac{1}{|s||t|} \mathcal{C}(v, s, t).$$

135 Since the normalized strength and densities are computable from the strength via a fixed
 136 normalization, our main statistical goal is to estimate $\mathcal{C}(v, s, t)$ for all v, s and t . In other words, we
 137 want to estimate matrices $\mathcal{C}_v \in \mathbb{R}_{\geq 0}^{S \times T}$. We call this estimator $\widehat{\mathcal{C}}$.

Construction of such an estimator raises the questions of what data to use for estimating which connectivity, how to featurize the dataset, what statistical estimator to use, and how to reconstruct the connectivity using the chosen estimator. Mathematically, we represent these considerations as

$$\widehat{\mathcal{C}}(v, s, t) = f^*(\widehat{f}(f_*(\mathcal{D}(v, s, t))). \quad (1)$$

138 This makes explicit the data featurization f_* , statistical estimator \widehat{f} , and any potential subsequent
 139 transformation f^* such as summing over the source and target regions. Denoting \mathcal{D} as a function of
 140 v, s , and t reflects that different data may be used to estimate different connectivities. Table 1 reviews
 141 estimators used for this data-type used in previous work, as well as our two main extensions: the
 142 **Cre-NW** and **Expected Loss** (EL) models. Additional information on these estimators is given in
 143 Supplemental Section ??.

Name	f^*	\hat{f}	f_*	$\mathcal{D}(v, s)$
NNLS (?)	$\hat{f}(S)$	NNLS(X,Y)	$X = x_{\mathcal{S}}, Y = y_{\mathcal{T}}$	I_m/I_m
NW (?)	$\sum_{l_s \in s} \hat{f}(l_s)$	NW(X,Y)	$X = c, Y = y_{\mathcal{T}}$	I_m/I_m
Cre-NW	$\sum_{l_s \in s} \hat{f}(l_s)$	NW(X,Y)	$X = c, Y = y_{\mathcal{T}}$	$(I_l \cap I_v)/I_m$
Expected Loss (EL)	$\sum_{l_s \in s} \hat{f}(s)$	EL(X, Y, v)	$X = c, Y = y_{\mathcal{T}}, v$	I_l/I_m

Table 1: Estimation of \mathcal{C} using connectivity data. The regionalization, estimation, and featurization steps are denoted by f^* , \hat{f} , and f_* , respectively. The training data used to fit the model is given by index set I . We denote experiments with centroids in particular major brain divisions and leaves as I_m and I_l , respectively. Data I_l/I_m means that, given a location $l_s \in s \in m$, the model \hat{f} is trained on all of I_m , but only uses I_l for prediction. The non-negative least squares estimator (NNLS) fits a linear model that predicts structural projection signal as a function of structural injection signal. It generates estimated connectivities for individual structures. The Nadaraya-Watson model (NW) is a local smoothing model that generates a prediction for each voxel within a structure. These predictions are averaged to create estimate the structure-specific connectivity.

144 Our contributions have several differences from the previous methods. In contrast to the
 145 non-negative least squares (?) and Nadaraya-Watson (?) estimators that take into account sources s
 146 and targets t , but not cell classes v , our new estimators specifically account for cell class. The Cre-NW
 147 estimator only uses experiments from a particular class to predict connectivity for that class, while the
 148 EL estimator shares information between classes within a structure. A detailed mathematical
 149 description of our new estimator is given in Supplemental Section ???. This estimator takes into
 150 account two types of covariate information about each experiment: the centroid of the injection, and
 151 the Cre-line. Like the NW and Cre-NW estimator, the EL estimator generates predictions for each
 152 voxel in a structure, and then sums them together to get the overall connectivity. However, in contrast
 153 to these alternative approaches, when predicting the projection pattern of a certain cell-class at a
 154 particular location, the EL estimator weights the average behavior of the class in the structure
 155 containing the location in question against the locations of the various nearby experiments. Thus,

¹⁵⁶ nearby experiments with similar Cre-lines can help generate the prediction, even when there are few
¹⁵⁷ nearby experiments of the cell-class in question.

158 ***Model evaluation***

159 We select optimum functions from within and between our estimator classes using **leave-one-out**
 160 **cross validation**, in which the accuracy of the model is assessed by its ability to predict experiments
 161 excluded from the training data. Equation 1 includes a deterministic step f^* included without input
 162 by the data. The performance of $\widehat{\mathcal{C}}(v, s, t)$ is thus determined by performance of $\widehat{f}(f_*(\mathcal{D}(v, s)))$. Thus,
 163 we can evaluate prediction on $f_{\mathcal{T}} : \mathbb{R}^3 \rightarrow \mathbb{R}_{\geq 0}^T$ - the regionalized connection strength at a given location.

164 Another question is what combinations of v , s , and t to generate a prediction for. Our EL and
 165 Cre-NW models are leaf specific. They only generate predictions for cell classes in leafs where at least
 166 one experiment with a Cre-line targeting that class has a centroid. To accurately compare our new
 167 estimators with less-restrictive models such as used in ?, we restrict our evaluation set to Cre
 168 driver/leaf combinations that are present at least twice. The sizes of these evaluation sets are given in
 169 Supplemental Section 5.

We use weighted l_2 -loss to evaluate these predictions.

$$\text{l2-loss } \ell(y_{\mathcal{T}}(i), \widehat{y_{\mathcal{T}}(i)}) := \|y_{\mathcal{T}}(i) - \widehat{y_{\mathcal{T}}(i)}\|_2^2.$$

$$\text{weighted l2-loss } \mathcal{L}(\widehat{f}(f_*)) := \frac{1}{|\{\mathcal{S}, \mathcal{V}\}|} \sum_{s, v \in \{\mathcal{S}, \mathcal{V}\}} \frac{1}{|I_s \cap I_v|} \sum_{i \in (I_s \cap I_v)} \ell(y_{\mathcal{T}}(i), \widehat{f}_{\mathcal{T}}(f_*(\mathcal{D}(v, s) \setminus i))).$$

170 This is a somewhat different loss from ?, both because of the normalization of projection, and because
 171 of the increased weighting of rarer combinations of s and v implicit in the $\frac{1}{|I_s \cap I_v|}$ term in the loss. As a
 172 final modeling step, we establish a lower limit of detection. The EL model also contains a separate
 173 cross-validation step. These approaches are covered in Supplemental Section ??

174 ***Connectivity analyses***

175 We examine latent structure underlying our estimated connectome using two types of unsupervised
 176 learning. Our use of hierarchical clustering is standard, and so we do not review it here. However, our
 177 application of non-negative matrix factorization (NMF) to decompose the estimated long-range
 178 connectivity into **connectivity archetypes** that linearly combine to reproduce the observed
 179 connectivity of some independent interest. Non-negative matrix factorization refers to a collection of
 180 **dictionary-learning** algorithms for decomposing a non-negatively-valued matrix such as \mathcal{C} into
 181 positively-valued matrices called, by convention, weights $W \in \mathbb{R}_{\geq 0}^{S \times q}$ and hidden units $H \in \mathbb{R}_{\geq 0}^{q \times T}$.
 182 Unlike PCA, NMF specifically accounts for the fact that data are all in the positive orthant. The matrix
 183 H is typically used to identify latent structures with interpretable biological meaning, and the choice
 184 of matrix factorization method reflects particular scientific subquestions and probabilistic
 185 interpretations.

186 Our algorithm solves the following optimization problem

$$\text{NMF}(\mathcal{C}, \lambda, q) := \arg \min_{W \in \mathbb{R}_{\geq 0}^{S \times q}, H \in \mathbb{R}_{\geq 0}^{q \times T}} \frac{1}{2} \| \mathbf{1}_{d(s,t) > 1500\mu m} \odot \mathcal{C} - WH \|_2^2 + \lambda (\|H\|_1 + \|W\|_1).$$

187 For this decomposition we ignore connections between source and target regions less than $1500\mu m$
 188 apart. This is because short-range projections resulting from diffusion dominate the matrices $\hat{\mathcal{C}}$, and
 189 represent a less-interesting type of biological structure. We set $\lambda = 0.002$ to encourage sparser and
 190 therefore more interpretable components. We use unsupervised cross-validation to determine an
 191 optimum q , and show the top 15 stable components (?). Stability analysis accounts for the
 192 difficult-to-optimize NMF program by clustering the resultant H from multiple replicates. Since the
 193 NMF objective is difficult to optimize and sensitive to initialization, we follow up with a stability
 194 analysis. The medians of the component clusters appearing frequently across NMF replicates are
 195 selected as **connectivity archetypes**. Details of these approaches are given in Supplementary Sections
 196 ?? and ??.

3 RESULTS

¹⁹⁷ We provide several types of results. First, we show that the novel expected-loss (EL) estimator
¹⁹⁸ performs best in our validation assays. Second, qualitative exploratory analysis confirms that the
¹⁹⁹ Cre-specific connectivity matrices generated using this model are consistent with known biology.
²⁰⁰ Third, statistical decomposition of the wild-type connectivity matrix using unsupervised learning
²⁰¹ shows how archetypal components can combine to produce observed signals.

²⁰² ***Model evaluation***

²⁰³ Our EL model generally performs better than the other estimators that we consider. Table 2 contains
²⁰⁴ weighted losses from leave-one-out cross-validation of candidate models, such as the NW Major-WT
²⁰⁵ model from ?. The EL model combines the good performance of class-specific models like NW
²⁰⁶ Leaf-Cre in regions like Isocortex with the good performance of class-agnostic models in regions like
²⁰⁷ Thalamus. Additional information on model evaluation, including class and structure specific
²⁰⁸ performance, is given in Appendix 5. In particular, Supplementary Table 4 contains the sizes of these
²⁰⁹ evaluation sets in each major structure, and Supplementary Section ?? contains the structure- and
²¹⁰ class specific losses.

	Mean Leaf-Cre	NW Major-Cre	NW Leaf-Cre	NW Leaf	NW Major-WT	NW Major	EL
\hat{f}	Mean	NW	NW	NW	NW	NW	EL
\mathcal{D}	$I_c \cap I_L$	$I_c \cap I_M$	$I_c \cap I_L$	I_L	$I_{wt} \cap I_M$	I_M	I_L
Isocortex	0.239	0.252	0.234	0.279	0.274	0.274	0.228
OLF	0.193	0.233	0.191	0.135	0.179	0.179	0.138
HPF	0.175	0.332	0.170	0.205	0.228	0.228	0.153
CTXsp	0.621	0.621	0.621	0.621	0.621	0.621	0.621
STR	0.131	0.121	0.128	0.169	0.232	0.232	0.124
PAL	0.203	0.205	0.203	0.295	0.291	0.291	0.188
TH	0.673	0.664	0.673	0.358	0.379	0.379	0.369
HY	0.360	0.382	0.353	0.337	0.317	0.317	0.311
MB	0.168	0.191	0.160	0.199	0.202	0.202	0.159
P	0.292	0.292	0.292	0.299	0.299	0.299	0.287
MY	0.268	0.347	0.268	0.190	0.189	0.189	0.204
CB	0.062	0.062	0.062	0.068	0.112	0.112	0.068

Table 2: Losses from leave-one-out cross-validation of candidate models. **Bold** numbers are best for their major structure.

211 ***Connectivities***

212 Our main result is the estimation of matrices $\hat{\mathcal{C}}_v \in \mathbb{R}_{\geq 0}^{S \times T}$ representing connections of source structures
 213 to target structures for particular cre-lines v . We confirm the detection of several well-established
 214 connectivities within our tensor, although it is our expectation that additional interesting biological
 215 processes are also manifest. The connectivity tensor and code to reproduce it are available at
 216 https://github.com/AllenInstitute/mouse_connectivity_models/tree/2020.

217 *Overall connectivity* Several expected biological projection patterns are evident in the wild-type
 218 connectivity matrix \mathcal{C}_{wt} from leaf sources to leaf targets shown in Figure 2a. Intraareal connectivities
 219 are clear, as are ipsilateral connections between cortex and thalamus. The clear intrastructural and
 220 intraareal connectivities mirror previous estimates in ? and ? and descriptive depictions of individual
 221 experiments in ?.

222 Our estimated wild-type connectivities appear more variable than those in ?, which used the NW
 223 Major-WT model whose accuracy is evaluated in Table 2. This is plausibly because of both the
 224 layer-specific targeting of the different cre-lines, and also the layer-specificity of the selected model.
 225 Although layer-specificity is a major advantage of including distinct cre-lines, for comparison, we also
 226 plot coarser projections between summary-structure sources and targets in the cortex in Figure 2b.
 227 These are averages over component layers weighted by layer size. Grossly congruent with the previous
 228 work, these results also exhibit a larger range of connectivities than those in ?. Importantly, as shown
 229 in Table 2 this finer spatial resolution corresponds to the increased accuracy of our EL model over the
 230 NW Major-WT model.

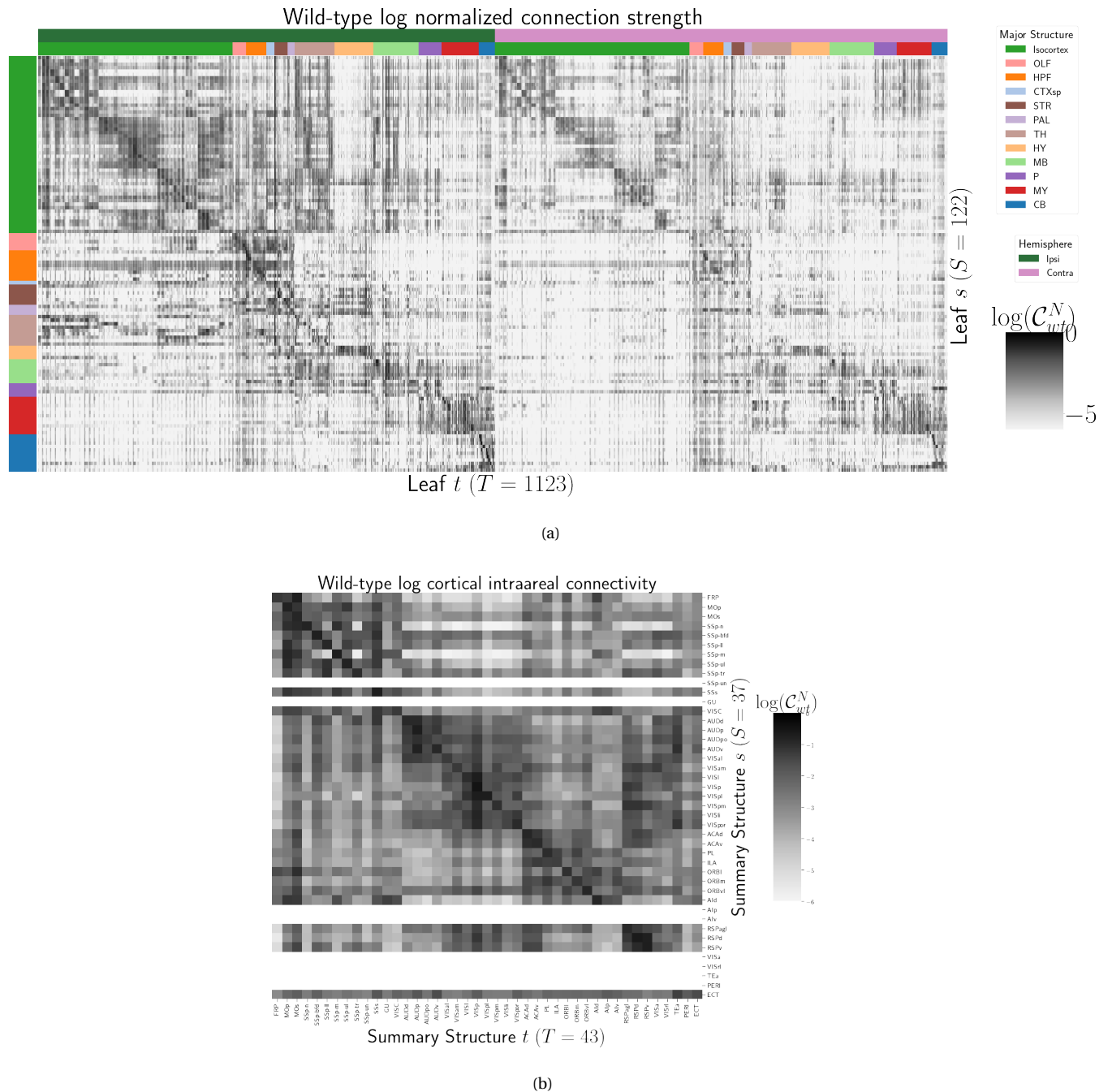


Figure 2: Wild-type connectivities. 2a Log wild-type connectivity matrix $\log \mathcal{C}(s, t, v_{wt})$. 2b Log wild-type intracortical connectivity matrix at the summary structure level.

231 *Class-specific connectivities* Source and cell-type combinations which project similarly indicate the
 232 network structure underpinning cognition. Although there is a rich anatomical literature using
 233 anterograde tracing data to describe projection patterns from subcortical sources to a small set of
 234 targets of interest, most accessible whole brain projection data are from the Allen Mouse Connectivity
 235 Atlas (MCA) project used here to generate the connectome models. Thus, to validate our results while
 236 avoiding a circular validation of the data used to generate the model weights, we confirm that these
 237 class-specific connectivities exhibit certain known behaviors. In particular, we focus on several cell
 238 types and source areas with extensive previous anatomical descriptions of projections using both bulk
 239 tracer methods with cell type specificity and single cell reconstructions: 1) thalamic-projecting
 240 neurons in the visual and motor cortical regions, 2) cholinergic neurons in the medial septum and
 241 nucleus of the diagonal band (MS/NDB); 3) cholinergic neurons in the caudoputamen, and 4)
 242 serotonergic neurons of the dorsal raphe nucleus (DR). We find that our inferred connections are in
 243 agreement with literature on these cell types.

244 DEPENDENCE OF THALAMIC CONNECTION ON CORTICAL LAYER. Visual cortical areas VIsP and VIsL and
 245 cortical motor areas MOp and MOs are ideal testbeds for our connectivities because there are
 246 well-established layer-specific projection patterns that can be labeled with the layer-specific cre-lines
 247 from the Allen datasets and others ??, and are also well-represented in our dataset. Figure 3a shows
 248 that in VIsP, the Ntsr1-Cre line strongly targets the core part of the thalamic LGd nucleus while in VIsL
 249 has a very strong projection to the LP nucleus. In VIsP, the Rbp4-Cre strongly targets LP as well.
 250 Recall that we display connectivity estimates for structures with at least one injection centroid in the
 251 structure. Thus, the position of non-zero rows in Figure 3a shows the localization of Rbp4-Cre and
 252 Ntsr1-Cre injection centroids to layers 5 and 6 respectively. This is further examined in Supplemental
 253 Section ??). Thus, as a heuristic alternative model, to also synthesize information about leafs targeted
 254 by different cre-lines, we also display an average connectivity matrix over all cre-lines. This combined
 255 output is not evaluated in our testing, and is only a general stand-in for overall behavior, but provides
 256 a useful summary of results.

257 MS AND NDB PROJECTIONS IN THE CHAT-IRES-CRE-NEO MODEL. Cholinergic neurons in the MS and
 258 NDB are well-known to strongly innervate the hippocampus, olfactory bulb, piriform cortex,
 259 entorhinal cortex, and lateral hypothalamus (??). In the Allen MCA, cholinergic neurons were labeled

260 by injections into Chat-IRES-Cre-neo mice. We first checked the estimated connectome weights to
 261 targets in these major brain divisions from MS and NDB. We observed that all these expected divisions
 262 were represented above the 90th percentile of weights. Recently, a single cell whole brain mapping
 263 project using Chat-Cre mice fully reconstructed n=50 cells, revealing these same major targets and
 264 also naming additional targets from MS/NDB (?). We compared our Chat-IRES-Cre connectome
 265 model data for MS and NDB with the targets identified by ?. We identified 150 targets at the fine leaf
 266 structure level in the top 10% of estimated weights. To directly compare our data across studies, we
 267 had to merge structures as needed to get to the same ontology level and remove ipsilateral and
 268 contralateral information. After formatting our data, we found 51 targets in the top 10%; Li et al.
 269 reported 47 targets across the 50 cells. There was good consistency overall between the target sets; 35
 270 targets were shared, 12 were unique to the single cell dataset, and 16 unique to our model data. We
 271 checked whether targets missing from our dataset were because of the threshold level. Indeed,
 272 lowering the threshold to the 75 th percentile confirmed 6 more targets-in-common, and all but 2
 273 targets from ? were above the 50th percentile weights in our model. Of note, the absence of a target in
 274 the single cell dataset that was identified in our model data is most likely due to the sparse sampling
 275 of all possible projections from only n=50 MS/NDB cells.

276 CP PROJECTIONS IN THE CHAT-IRES-CRE-NEO MODEL. Most cells in the caudoputamen (CP) are
 277 GABAergic spiny projection neurons. These cells are also the only type that send projections outside
 278 the CP. Cholinergic interneurons make up 1-2% of all CP cells and their axon terminals do not extend
 279 beyond the CP borders. We confirmed that the model predictions for connection weights from CP
 280 cholinergic cells were consistent with this known anatomy; the connection weight to CP was ~ 2-fold
 281 higher than any other in the top 5%.

282 DR PROJECTIONS IN THE SLC6A4-CRE'ET33 MODEL. Serotonergic projections from cells in the
 283 dorsal raphe (DR) are widely distributed and innervate many forebrain structures including isocortex
 284 and amygdala. In the Allen MCA, serotonergic neurons were labeled using Slc6a4-Cre_ET33 and
 285 Slc6a4-CreERT2_EZ13 mice. This small nucleus appears to contain a complex mix of molecularly
 286 distinct serotonergic neuron subtypes with some hints of subtype-specific projection patterns (???).
 287 We expect that the Cre lines we used here in the Allen MCA, which utilize the serotonin transporter
 288 promoter (Slc6a4-Cre and -CreERT2), will lead to expression of tracer in all the serotonergic subtypes

289 recently described in an unbiased way, but this assumption has not been tested directly. We
290 compared our model data to a single cell reconstruction dataset consisting of n=50 serotonergic cells
291 with somas in the DR that also had bulk tracer validation ([SK's comment:INSERT LINK TO FIGURE](#)). ?
292 listed 55 targets across the single cell reconstructions. After processing our data to match the target
293 structure ontology level across studies, we identified 37 targets from the DR with weights above the 90
294 th percentile; 27 of these targets matched those named by ?. Overall there was good consistency
295 between targets in olfactory areas, cortical subplate, CP, ACB and amygdala areas, as well in pallidum
296 and midbrain.

297 The two major brain divisions with the least number of matches are the isocortex and thalamus.
298 There are a few likely reasons for these observations. First, in the isocortex, there is known to be
299 significant variation in the density of projections across different locations, with the strongest
300 innervation in lateral and frontal orbital cortices ???. Indeed, when we lower the threshold and check
301 for weights of the targets outside of the 90%, we see all but one of these regions (PTLp, parietal cortex
302 which is not frontal or lateral) has a weight assigned in the top half of all targets. In the thalamus, it
303 was also interesting to observe that our model predicted strong connections to several medial
304 thalamic nuclei (i.e., MD, SMT), that were not targeted by the single cells. This discrepancy may be at
305 least partially explained by the complex topographical organization of the DR that, like the molecular
306 subtypes, is not yet completely understood. A previous bulk tracer study that specifically targeted
307 injections to the central, lateral wings, and dorsal subregions of the DR reported semi-quantitative
308 differences in projection patterns (?). Notably, ? report that cells in the ventral region of DR project
309 more strongly to medial thalamic nuclei, whereas the lateral and dorsal DR cells innervate more lateral
310 regions (e.g., LGd). So it is possible that the single cell somas did not adequately sample the entire DR.

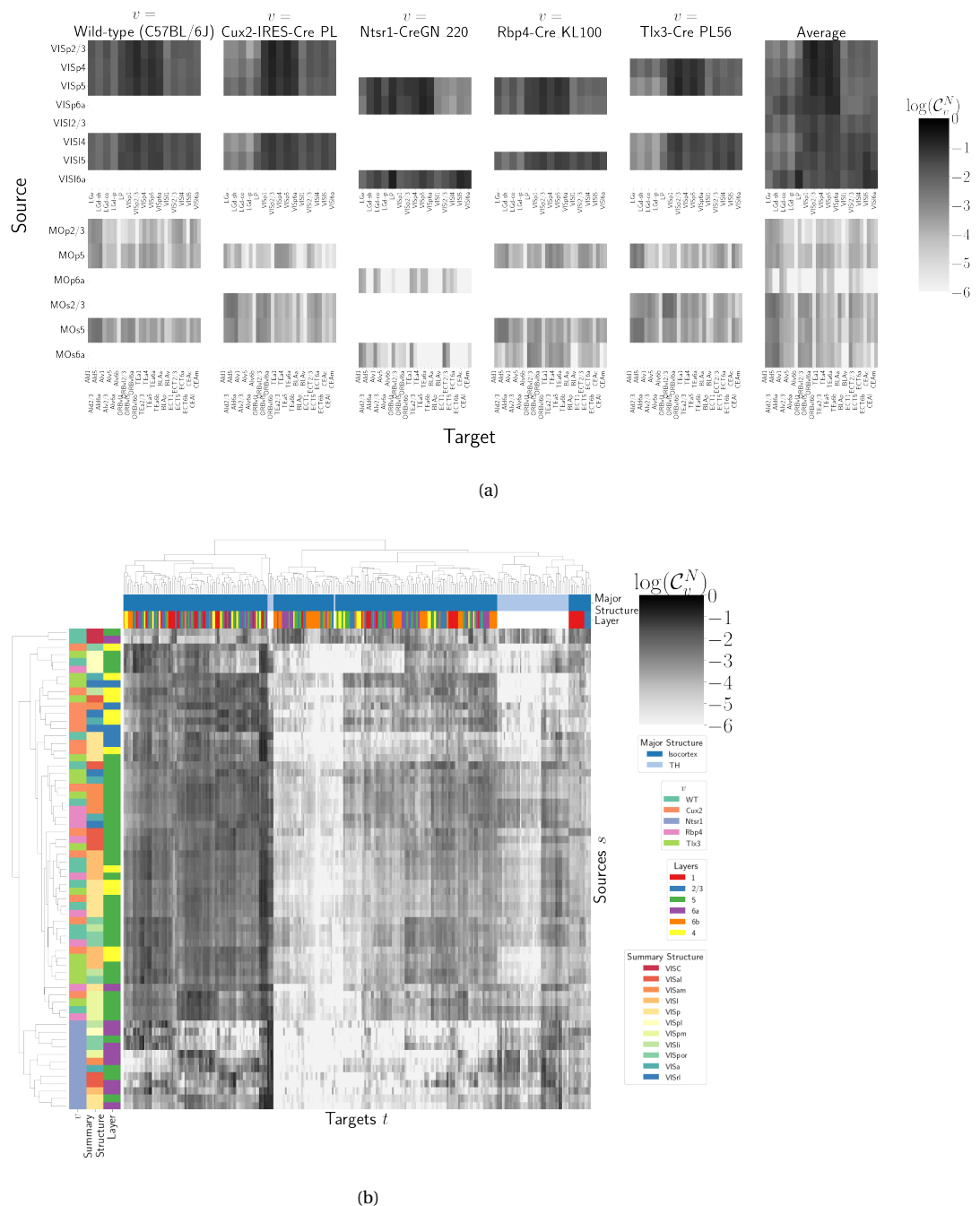


Figure 3: Cell-class specificity. 3a Selected cell-class and layer specific connectivities from two visual and two motor areas. Sources without an injection in the Cre driver line are not estimated due to lack of data for that Cre-line in that structure. 3b Hierarchical clustering of connectivity strengths from visual cortex cell-types to cortical and thalamic targets. Cre-line, summary structure, and layer are labelled on the sources. Major brain division and layer are labelled on the targets.

311 ***Connectivity Analyses***312 **(SK's comment:move to connectivity analysis section)**

313 Cell-class, while often correlated with cortical layer, can be a stronger driver of connectivity than
 314 summary structure especially when looking at targets at major brain division level. Figure 3b shows a
 315 collection of connectivity strengths generated using cre-specific models for wild-type, Cux2, Ntsr1,
 316 Rbp4, and Tlx3 cre-lines from VIS areas at leaf level in the cortex to cortical and thalamic nuclei. We
 317 use hierarchical clustering to sort source structure/cell-class combinations by the similarity of their
 318 structural projections, and sort target structures by the structures from which they receive projections.
 319 Examining the former, we can see that the layer 6 Ntsr1 Cre-line distinctly projects to thalamic nuclei,
 320 regardless of source summary structure. This contrasts with the tendency of other cell-classes to
 321 project intracortically in a manner determined by the source structure. Similarly, layer 6 targets are
 322 not strongly projected to by any of the displayed Cre-lines. There are too many targeted summary
 323 structures to plot here, but we expect that the source profile of each target clusters by structure.

324 Each regionalized connectivity matrix is a high-dimensional realization of relatively few biological
 325 processes, and decomposition of neural signals to recover these processes is a fundamental goal in
 326 neuroscience. In this section, we apply non-negative matrix factorization to decompose the
 327 long-range wild-type connectivities into linear combinations of archetypal connectivities. This
 328 decomposes the remaining censored connectivity matrix into a linear model based off a relatively
 329 small number of distinct signals. This model is able to capture a large amount of the observed
 330 variability, and recovers structure-specific archetypal signals.

331 These signals are plotted in Figure 4, and technical details and intermediate results are given in
 332 Supplemental Sections ?? and ??, respectively. These details include a cross-validation based method
 333 for selecting the number of components, a masking method for focusing only on long range
 334 connections, and a stability method for ensuring that the decomposition is reliable across
 335 computational replicates. The plotted decomposition shows that these underlying connectivity
 336 archetypes correspond strongly to major brain division in both target and sources.

337 Inspection of the reconstructed distal normalized connection strength using the top 15
 338 components shows qualitatively shows that this relatively sparse decomposition is able to capture

³³⁹ much of the observed variability. Other connectivity patterns like cortical-cortical and
³⁴⁰ cortical-thalamic are also detected.

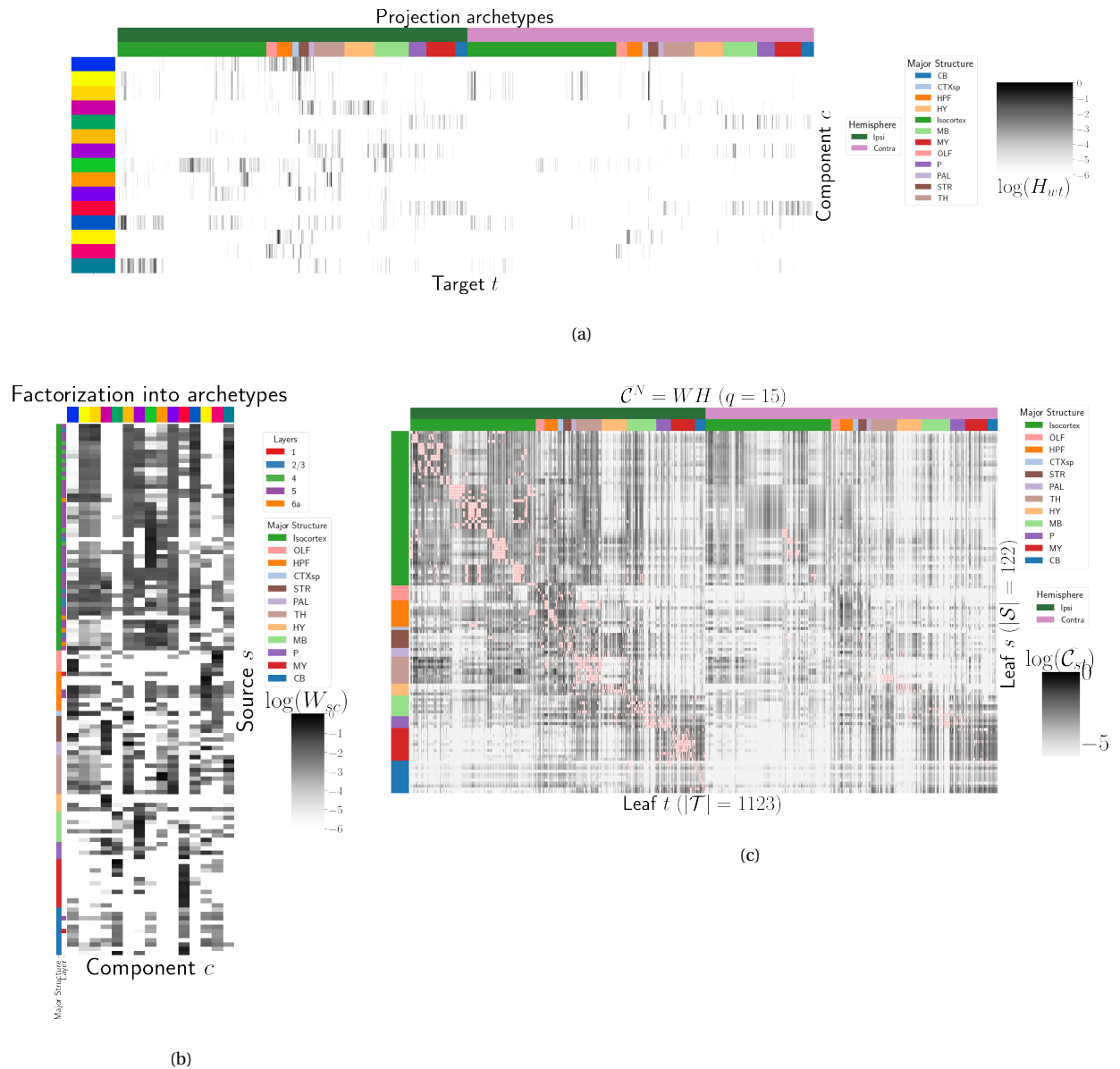


Figure 4: Non-negative matrix factorization results $\mathcal{C}_w^N = W H$ for $q = 15$ components. 4a Latent space coordinates H of \mathcal{C} . Target major structure and hemisphere are plotted. 4b Loading matrix W . Source major structure and layer are plotted. 4c Reconstruction of the normalized distal connectivity strength using the top 15 archetypes. Areas less than $1500 \mu\text{m}$ apart are not modeled, and therefore shown in red.

4 DISCUSSION

341 The model presented here is the first cell-type specific whole brain projectome model for a
 342 mammalian species, and it opens the door for a large number of models linking brain structure to
 343 computational architectures. Overall, we find expected targets, based on our anatomical expertise
 344 and published reports, but underscore that the core utility of this bulk connectivity analysis is not
 345 only in validation of existing connection patterns, but also in identification of new ones. We note that
 346 although the concordance appeared stronger for the cholinergic cells than the serotonergic cells, any
 347 differences might still be explained by the lack of high quality “ground-truth” datasets to validate
 348 these Cre connectome models. Larger numbers of single cell reconstructions, that saturate all
 349 possible projection types, would be a better gold standard than the small number of cells reported
 350 here (n=50 for each). ([SK's comment: add citation](#)) Perhaps future iterations of the connectome model
 351 may also take into account some single cell axon projection data.

352 The Nadaraya-Watson estimator presented here is novel. Beyond using a Nadaraya-Watson kernel
 353 regression defined in physical space, we define a cell-type space based on similarities of projections,
 354 and theoretically justify the use of an intermediate shape-constrained estimator. While methods like
 355 non-negative least squares can also account for covariates, the centroid method from ? was shown
 356 that the more precise notion of injection location than the non-negative least squares in ?.
 357 Furthermore, our sample size seems too low to utilize a fixed or mixed effect, particularly since the
 358 impact of the virus depend on the particular injection region. In a sense both the NNLS and NW
 359 models can be thought of as improvements over the structure-specific average, and so is also possible
 360 that a yet undeveloped residual-based data-driven blend of these models could provide improved
 361 performance.

362 We see several other opportunities for improving on our model. Ours is certainly not the first
 363 cross-validation based model averaging method ?. However, our use of shape-constrained estimator
 364 in target-encoded feature space is novel and fundamentally different from Nadaraya-Watson
 365 estimators that use an optimization method for selecting the weights (?). The properties of this
 366 estimator, as well as its relation to estimators fit using an optimization algorithm, are a possible future
 367 avenue of research. A deep model such as ? could be appropriate, provided enough data was
 368 available. Finally, a Wasserstein-based measure of injection similarity per structure would combine

369 both the physical simplicity of the centroid model while also incorporating the full distribution of the
370 injection signal.

371 The factorization of the connectivity matrix could also be improved and better used. From a
372 statistical perspective, stability-based method for establishing archetypal connectivities in NMF is
373 similar to those applied to genomic data ?? . However, non-linear data transformations or matrix
374 decompositions, or tensor factorizations that account for correlations between cell-types could better
375 capture the true nature of archetypal neural connections. It would also be of great interest to associate
376 the archetypal signals detected from connectivity analysis with undergirding gene expression patterns
377 or functional information.

ACKNOWLEDGMENTS

³⁷⁸ We thank the Allen Institute for Brain Science founder, Paul G. Allen, for his vision, encouragement,
³⁷⁹ and support.

380 This supplement is divided into information about our dataset, supplemental methods, and
381 supplemental results. However, certain topics are revisited between sections. Thus, if a reader is
382 interested in, say, non-negative matrix factorization, they may find relevant information in both
383 methods and results.

5 SUPPLEMENTAL INFORMATION

384 Our supplementary information consists of abundances of leaf/Cre-line combinations, information
385 about distances between structures, and the size of our restricted evaluation dataset.

386 *Cre/structure combinations in \mathcal{D}*

387 This section describes the abundances of leaf and Cre-line combinations in our dataset. Users of the
388 connectivity matrices who are interested in a particular Cre-line or structure can see the quantity and
389 type of data used to compute and evaluate that connectivity.

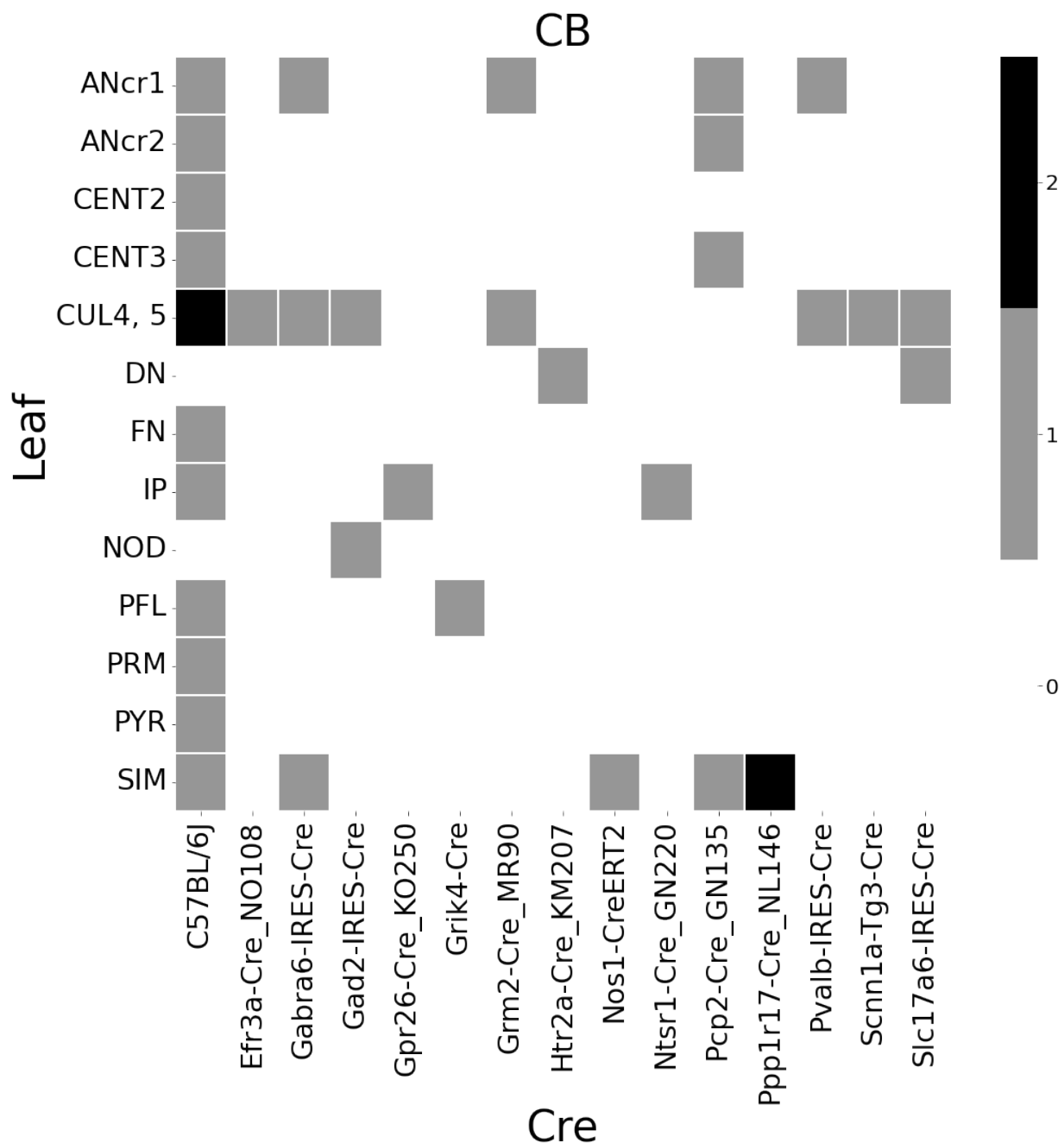


Figure 5: Abundances of Cre-line and leaf-centroid combinations.

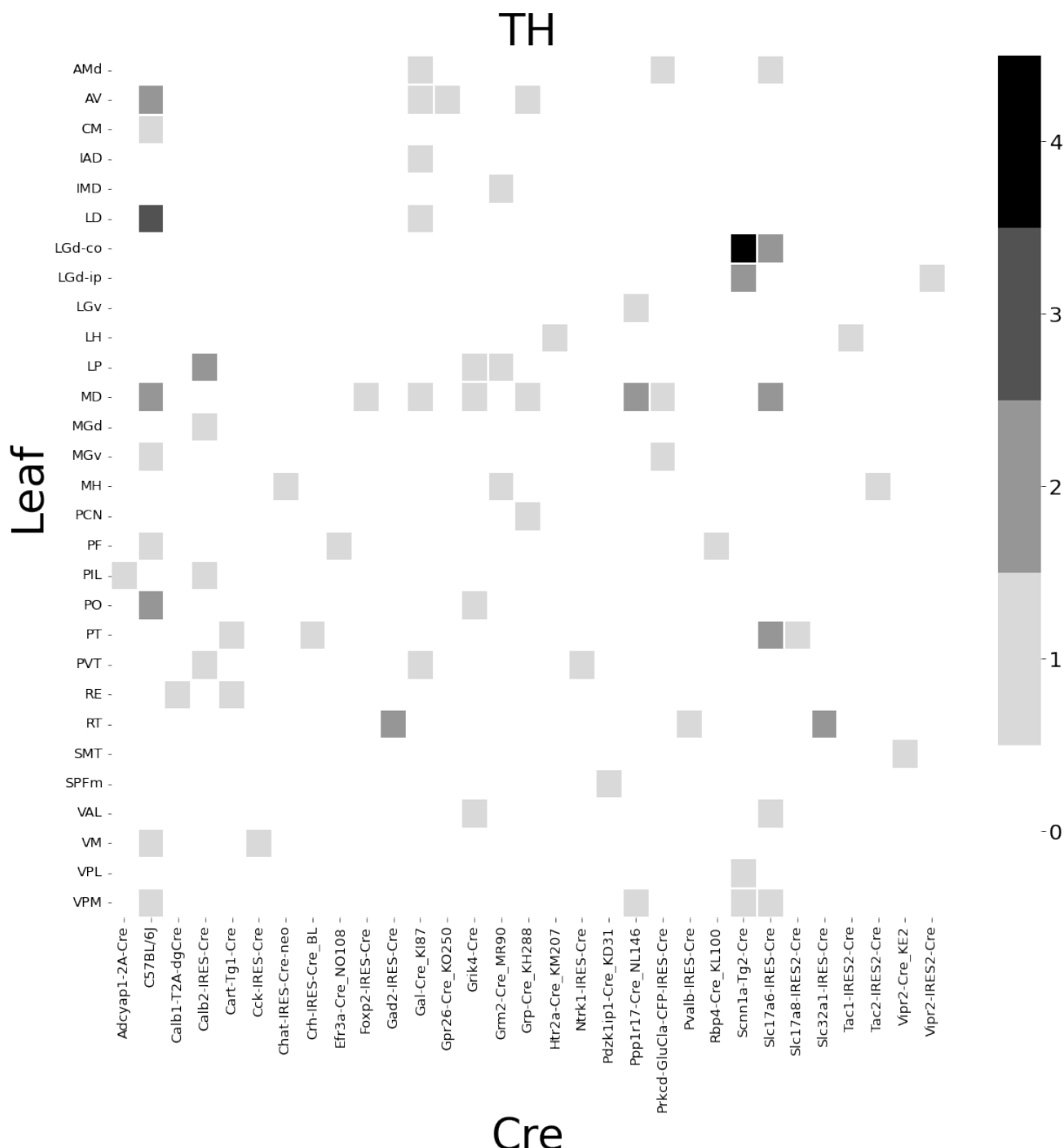


Figure 6: Abundances of Cre-line and leaf-centroid combinations.

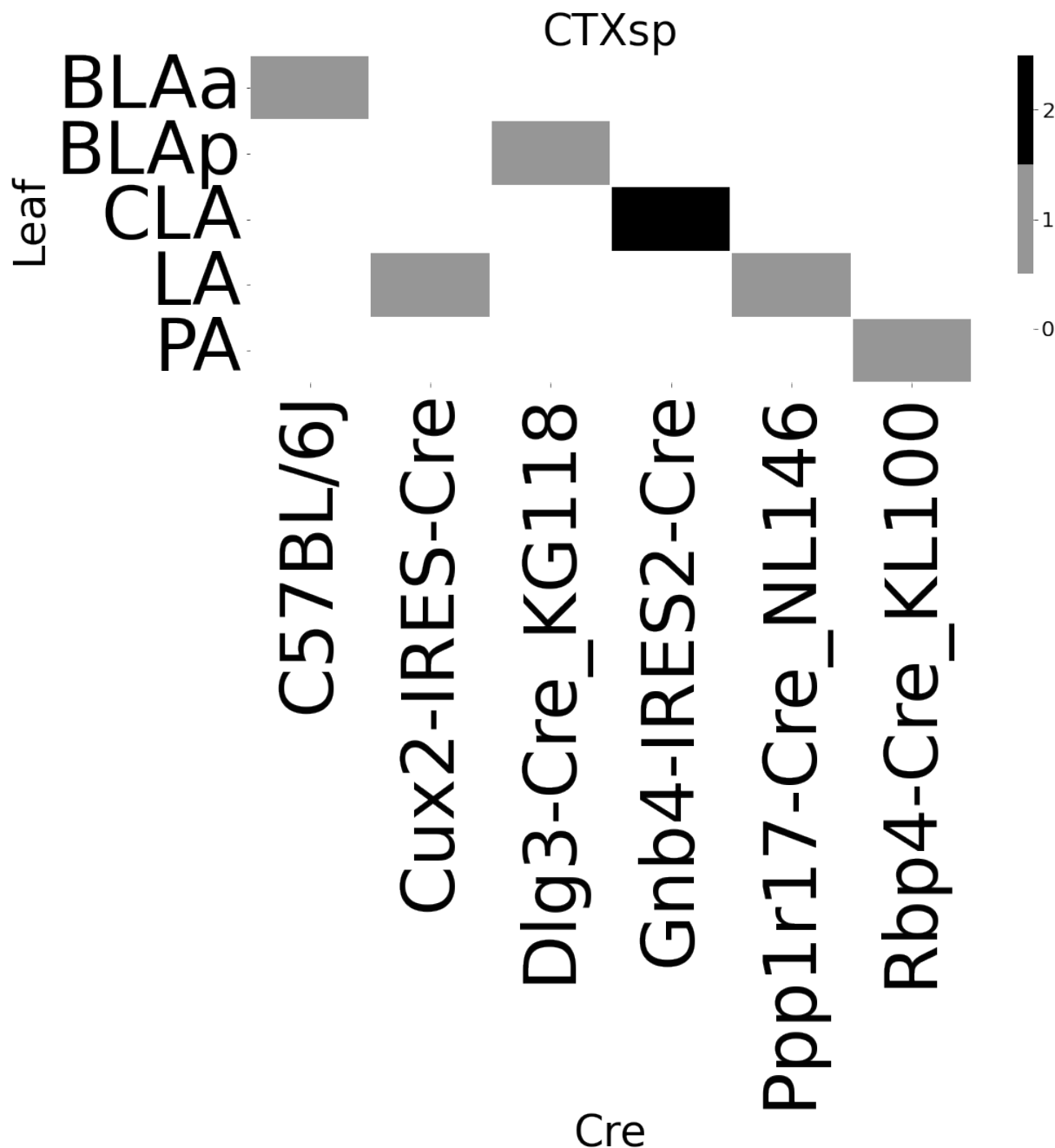


Figure 7: Abundances of Cre-line and leaf-centroid combinations.

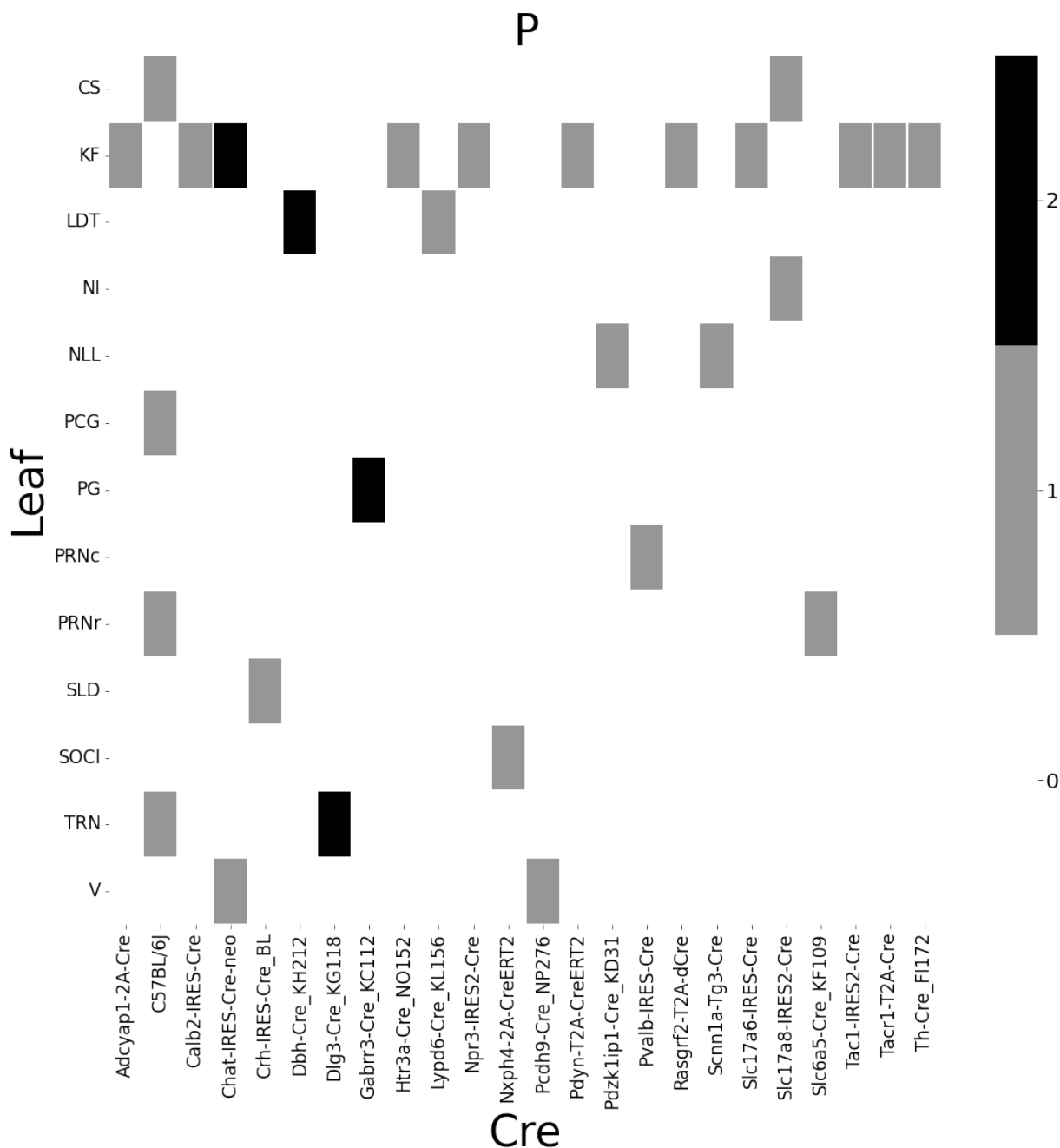


Figure 8: Abundances of cre-line and leaf-centroid combinations.

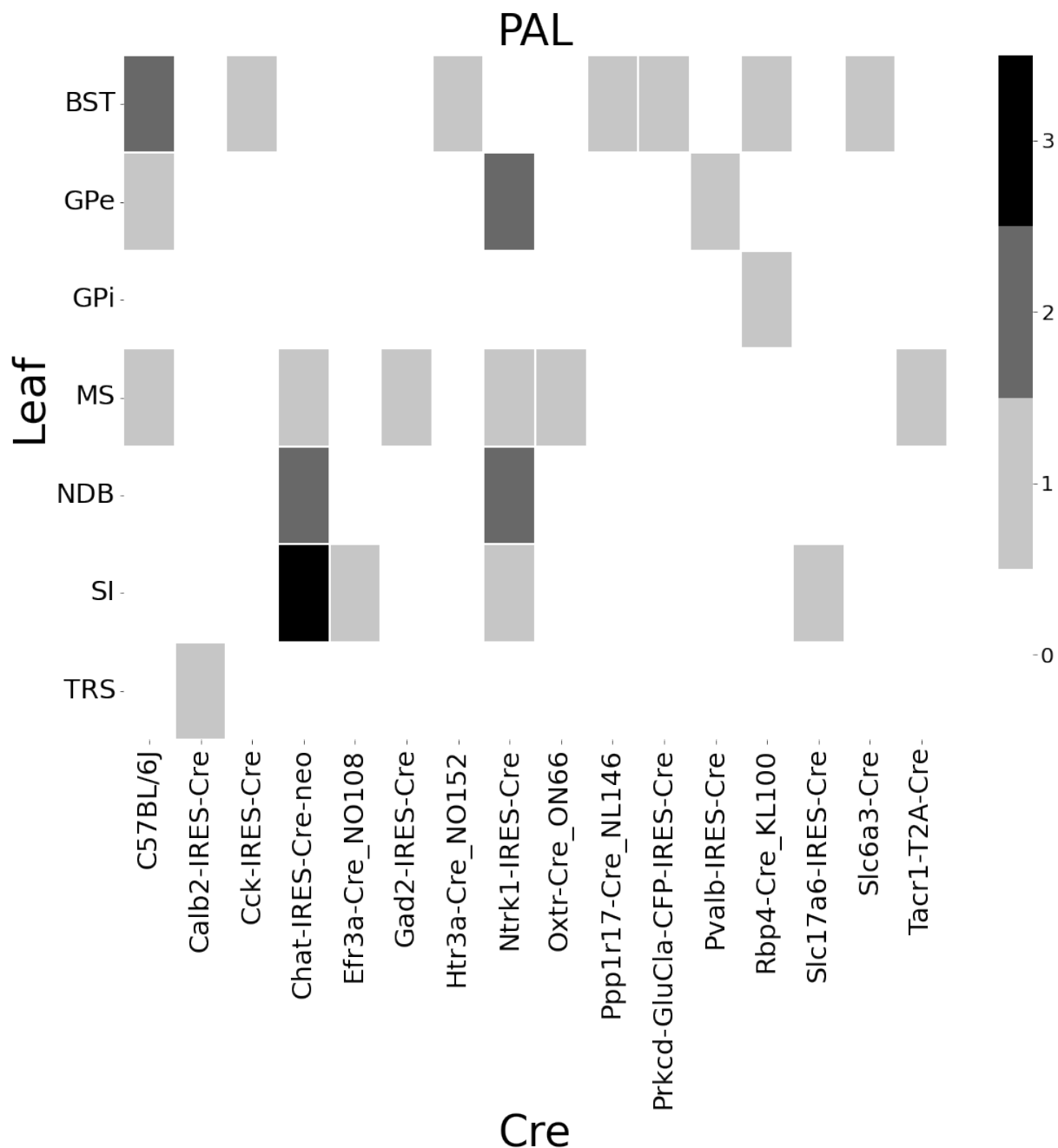


Figure 9: Abundances of Cre-line and leaf-centroid combinations.

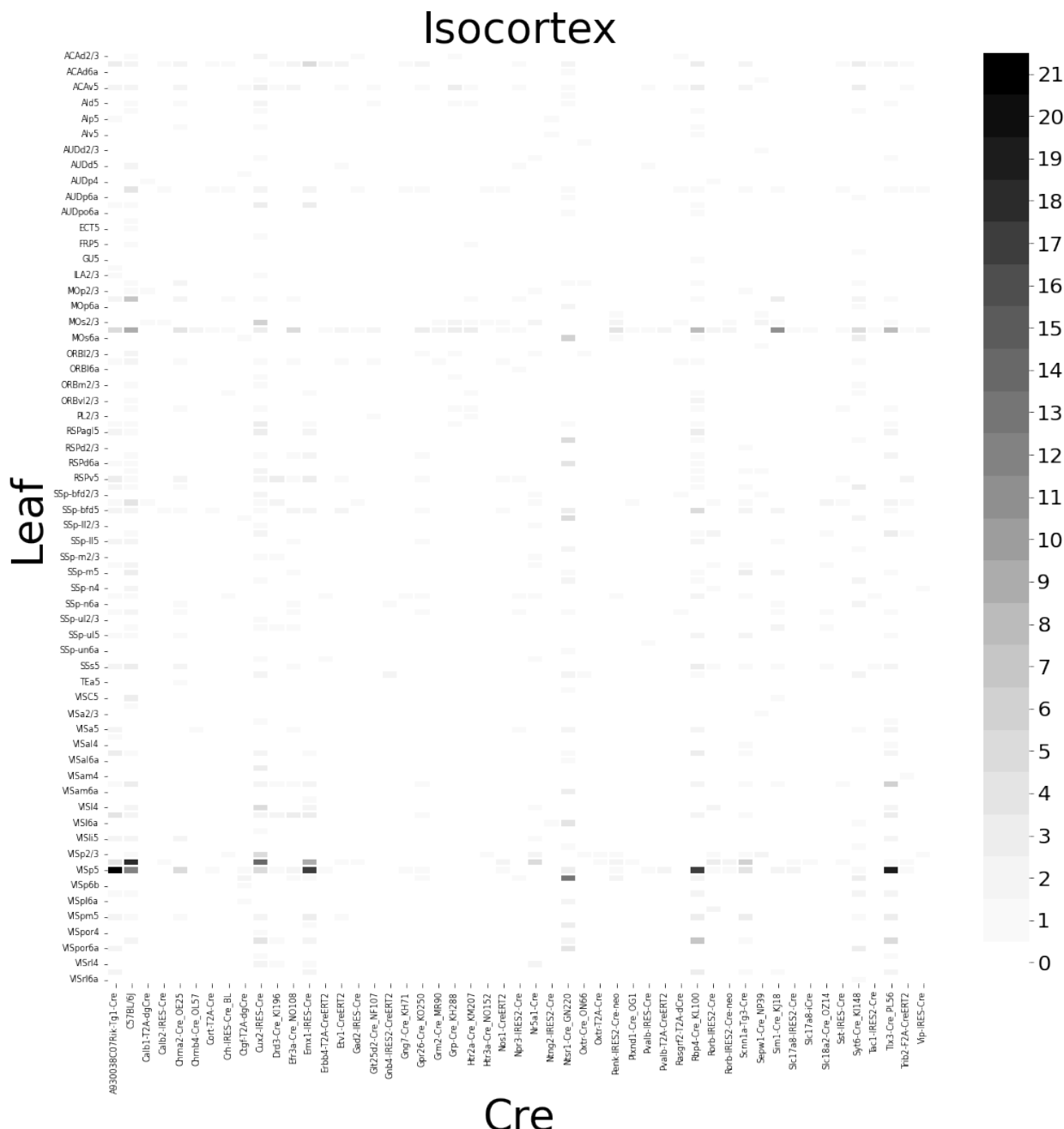


Figure 10: Abundances of Cre-line and leaf-centroid combinations.

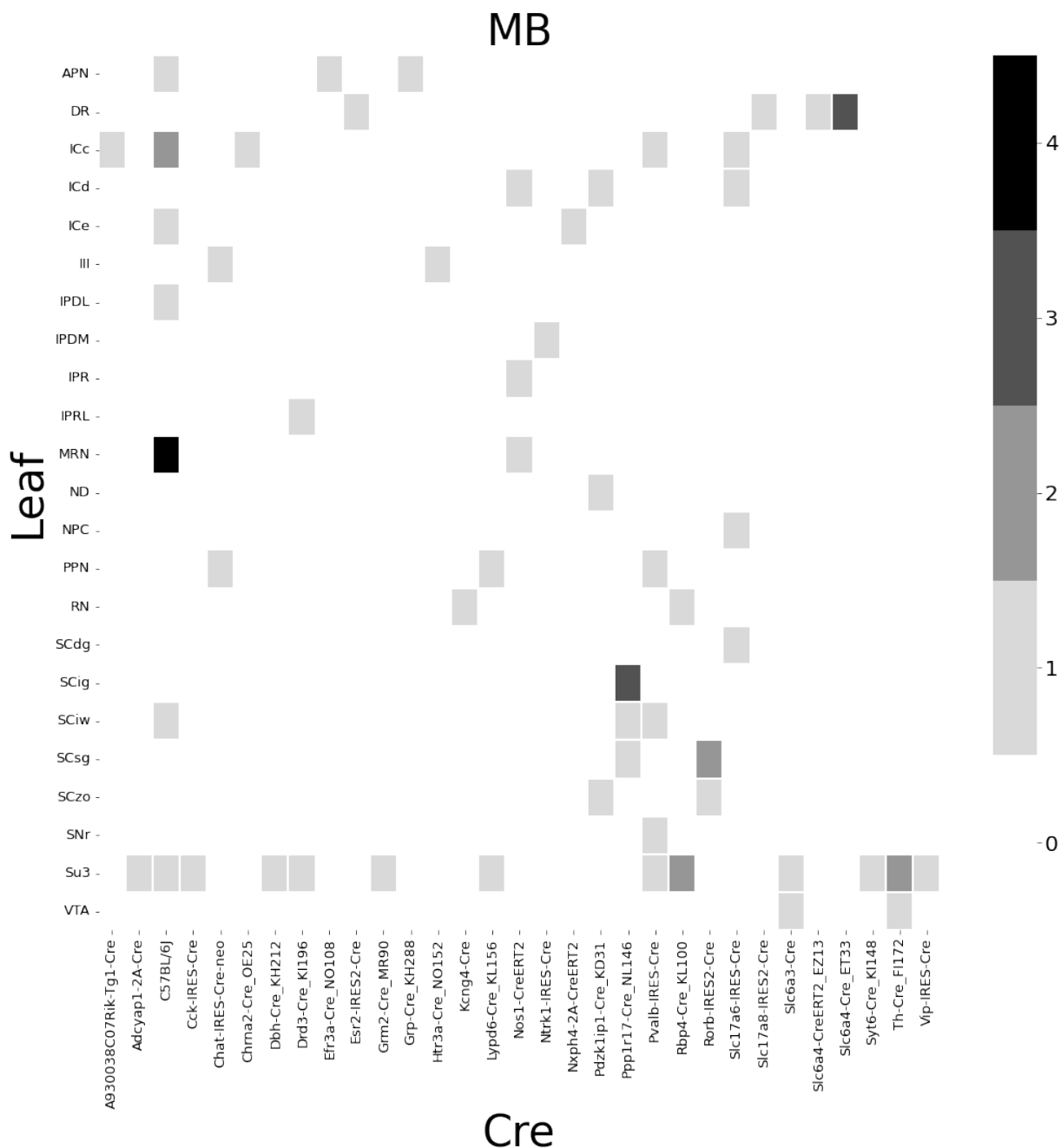


Figure 11: Abundances of Cre-line and leaf-centroid combinations.

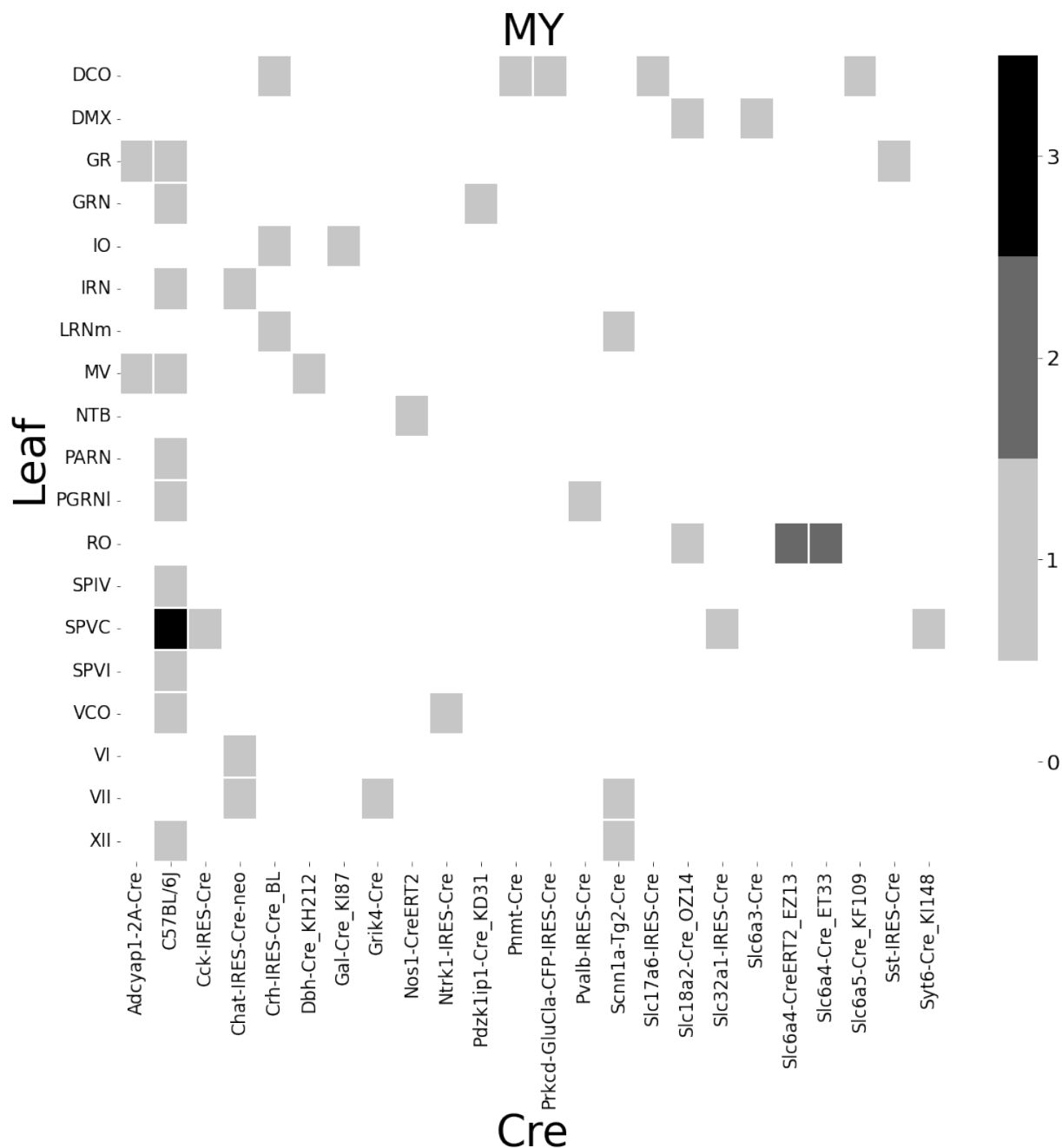
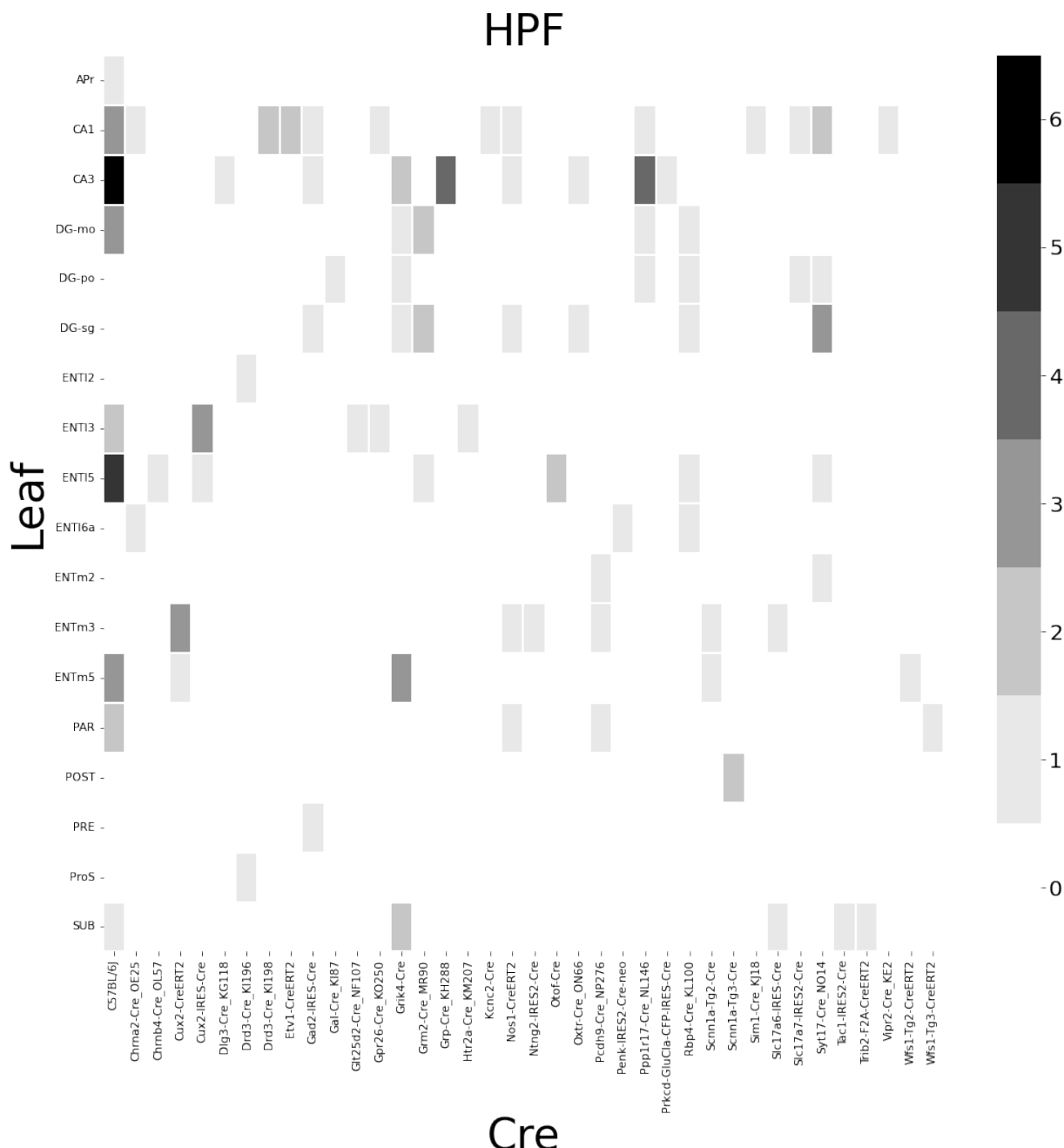


Figure 12: Abundances of Cre-line and leaf-centroid combinations.



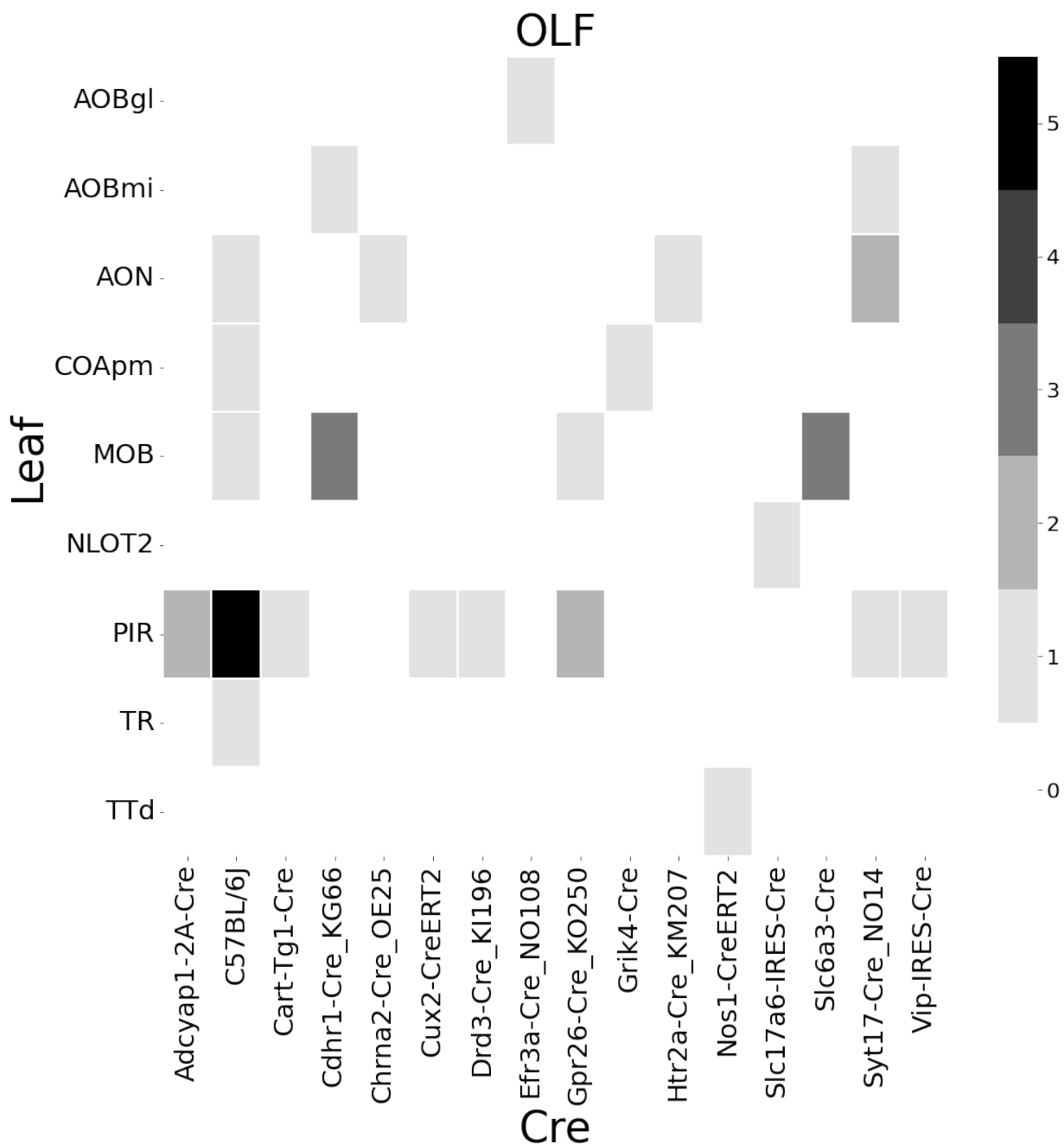


Figure 14: Abundances of Cre-line and leaf-centroid combinations.

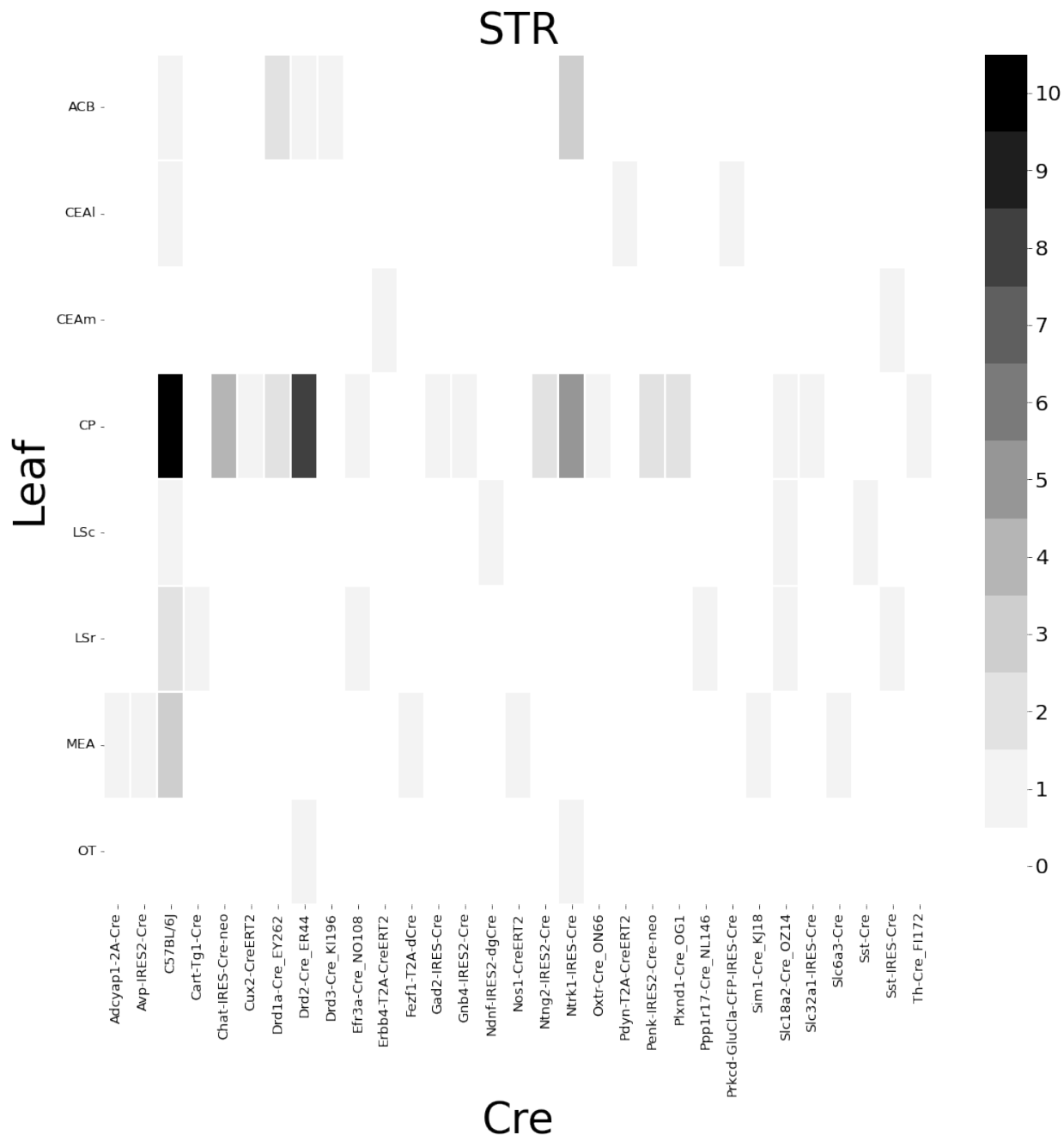


Figure 15: Abundances of Cre-line and leaf-centroid combinations.

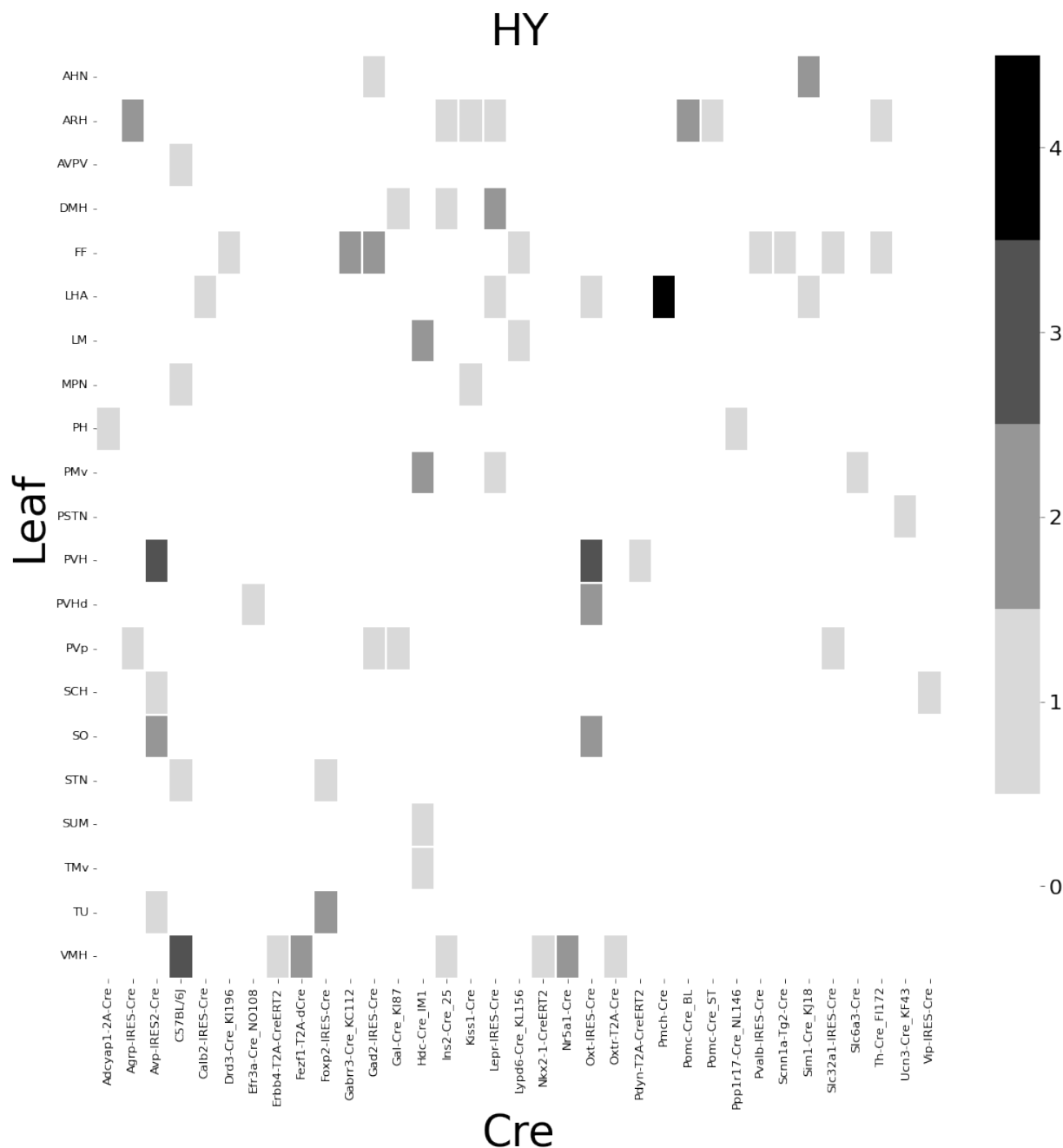


Figure 16: Abundances of Cre-line and leaf-centroid combinations.

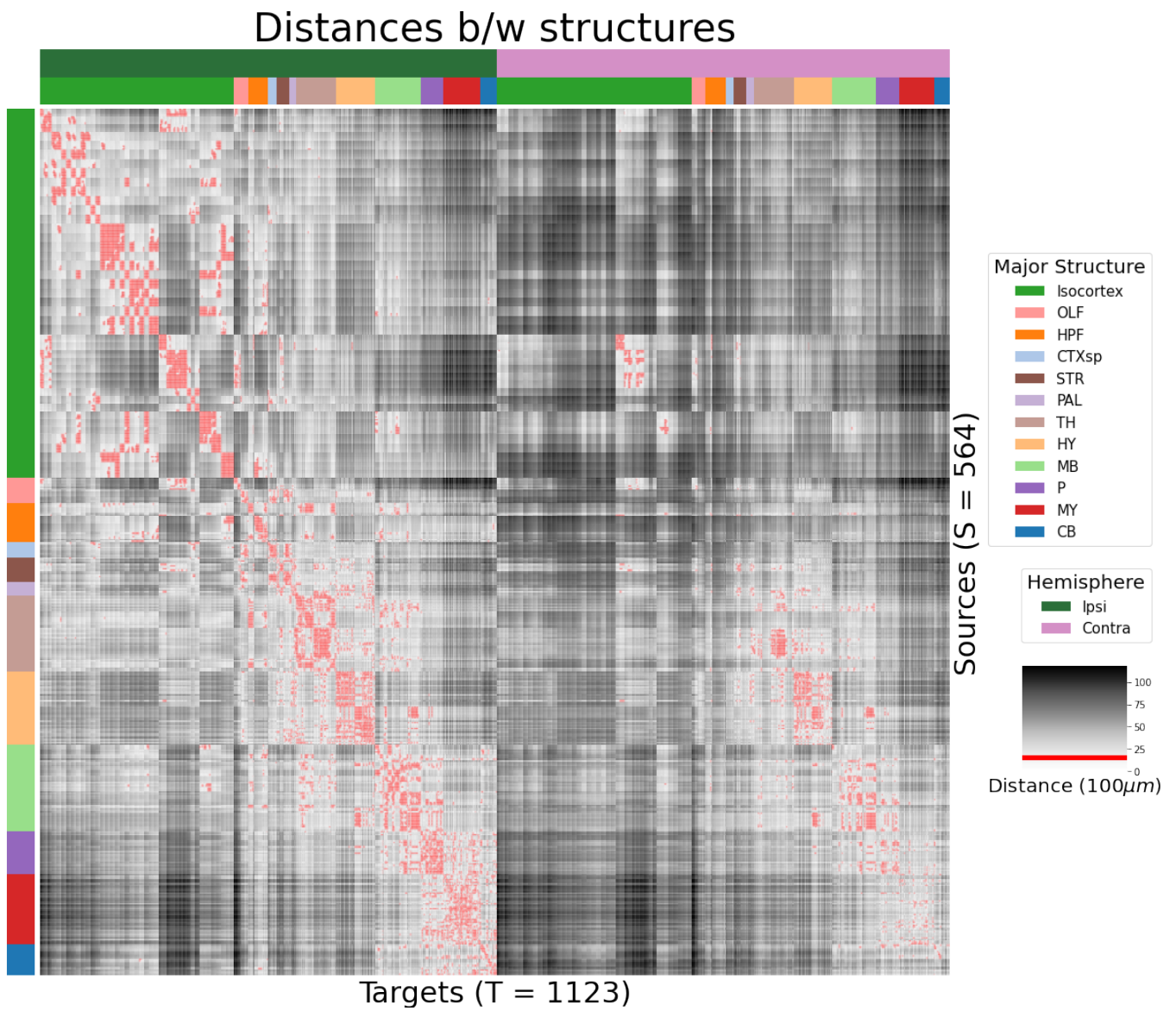
390 ***Distances between structures***

Figure 17: Distance between structures. Short-range connections are masked in red

391 ***Model evaluation***

392 We give information on the quality of our models. This includes the sizes of our evaluation sets in
 393 leave-one-out cross-validation and additional losses in the injection-normalized case.

394 NUMBER OF EXPERIMENTS IN EVALUATION SETS In order to compare between methods, we therefore
 395 restrict to the smallest set of evaluation indices, which is to say, virus-leaf combinations that are
 396 present at least twice. This means that our evaluation set is smaller in size than our overall list of
 397 experiments.

	Total	Cre-Leaf	Cre-leaf over threshold
Isocortex	36	4	4
OLF	7	2	2
HPF	122	62	59
CTXsp	85	41	38
STR	1128	732	7
PAL	68	18	17
TH	46	7	7
HY	35	17	17
MB	33	8	8
P	30	11	11
MY	78	45	44
CB	83	29	29

Table 3: Number of experiments available to evaluate models in leave-one-out cross validation. Models that rely on a finer granularity of modeling have less data available to validate with.

398 INJECTION-NORMALIZED LOSSES To compare with the injection-normalization procedure from ?, we
 399 also remove experiments with small injection, and here give results for this slightly reduced set using
 400 injection-normalization. That is, instead of dividing the projection signal of each experiment by its l_1
 401 norm, we divide by the l_1 norm of the corresponding injection signal. We find that setting a summed
 402 injection-signal of threshold of 1 is sufficient for evading pathological edge cases in this
 403 normalization, while still retaining a large evaluation set.

\hat{f}	Mean	NW					EL
\mathcal{D}	$I_c \cap I_L$	$I_c \cap I_M$	$I_c \cap I_L$	I_L	$I_{wt} \cap I_M$	I_M	I_L
Isocortex	0.413	0.453	0.408	0.538	0.528	0.528	0.396
OLF	0.499	0.504	0.494	0.441	0.543	0.543	0.437
HPF	0.336	0.483	0.332	0.444	0.501	0.501	0.321
CTXsp	0.497	0.497	0.497	0.497	0.497	0.497	0.497
STR	0.359	0.386	0.359	0.364	0.433	0.433	0.322
PAL	0.519	0.497	0.519	0.436	0.459	0.459	0.434
TH	0.769	0.767	0.769	0.514	0.539	0.539	0.556
HY	0.414	0.439	0.414	0.441	0.452	0.452	0.399
MB	0.459	0.396	0.397	0.358	0.324	0.324	0.403
P	0.562	0.562	0.562	0.758	0.764	0.764	0.562
MY	0.699	0.552	0.621	0.439	0.578	0.578	0.439
CB	0.849	0.689	0.849	0.500	0.615	0.615	0.495

Table 4: Losses from leave-one-out cross-validation of candidate for injection-normalized regionalized connectivity on injection-thresholded evaluation set. **Bold** numbers are best for their major structure.

404 PROJECTION-NORMALIZED LOSSES ON THRESHOLDED SET We also give results for the
 405 projection-normalization procedure from the main text on this reduced subset.

\hat{f}	Mean	NW	EL				
\mathcal{D}	$I_c \cap I_L$	$I_c \cap I_M$	$I_c \cap I_L$	I_L	$I_{wt} \cap I_M$	I_M	I_L
Isocortex	0.229	0.248	0.224	0.274	0.269	0.269	0.217
OLF	0.193	0.233	0.191	0.135	0.179	0.179	0.138
HPF	0.178	0.342	0.172	0.212	0.235	0.235	0.172
CTXsp	0.621	0.621	0.621	0.621	0.621	0.621	0.621
STR	0.128	0.117	0.124	0.171	0.234	0.234	0.125
PAL	0.203	0.205	0.203	0.295	0.291	0.291	0.188
TH	0.673	0.664	0.673	0.358	0.379	0.379	0.417
HY	0.358	0.378	0.351	0.331	0.312	0.312	0.314
MB	0.168	0.191	0.160	0.199	0.202	0.202	0.160
P	0.292	0.292	0.292	0.299	0.299	0.299	0.287
MY	0.268	0.347	0.268	0.167	0.189	0.189	0.196
CB	0.062	0.062	0.062	0.068	0.108	0.108	0.061

Table 5: Losses from leave-one-out cross-validation of candidate for normalized regionalized connectivity on injection-thresholded evaluation set. **Bold** numbers are best for their major structure.

6 SUPPLEMENTAL METHODS

⁴⁰⁶ This section consists of additional information on preprocessing of the neural connectivity data,
⁴⁰⁷ estimation of connectivity, and matrix factorization.

⁴⁰⁸ ***Data preprocessing***

⁴⁰⁹ Several data preprocessing steps take place prior to evaluations of the connectivity matrices. These
⁴¹⁰ steps are described in Algorithm PREPROCESS. The arguments of this normalization process - injection
⁴¹¹ signals $x(i)$, projection signals $y(i)$, injection fraction $F(i)$, and data quality mask $q(i)$ - were
⁴¹² downloaded using the Allen SDK. The injections and projection signals $\mathcal{B} \rightarrow [0, 1]$ were segmented
⁴¹³ manually in histological analysis. The projection signal gives the proportion of pixels within the voxel
⁴¹⁴ displaying fluorescence, and the injection signal gives the proportion of pixels within the
⁴¹⁵ histologically-selected injection subset displaying fluorescence. The injection fraction $\mathcal{B} \rightarrow [0, 1]$ gives
⁴¹⁶ the proportion of pixels within each voxel in the injection subset. Finally, the data quality mask
⁴¹⁷ $\mathcal{B} \rightarrow \{0, 1\}$ gives the voxels that have valid data.

⁴¹⁸ Our preprocessing makes use of the above ingredients, as well as several other essential steps. First,
⁴¹⁹ we compute the weighted injection centroid

$$c(i) = \sum_{l \in \mathcal{B}} x(l)l$$

⁴²⁰ where $x(i)(l)$ is the injection density at location $l \in \mathbb{R}^3$. Given a regionalization \mathcal{R} from the Allen SDK,
⁴²¹ we can also access regionalization map $R: \mathcal{B} \rightarrow \mathcal{R}$. This induces a functional of connectivities from
⁴²² the space of maps $\{\mathcal{X} = x: \mathcal{B} \rightarrow [0, 1]$

$$\begin{aligned} 1_{\mathcal{R}}: \mathcal{X} &\rightarrow \mathcal{R} \times \mathbb{R}_{\geq 0} \\ x &\mapsto \sum_{l \in r} x(l) \text{ for } r \in \mathcal{R}. \end{aligned}$$

⁴²³ We also can restrict a signal to a individual structure as

$$\begin{aligned} 1|_s: \mathcal{X} &\rightarrow \mathcal{X} \\ x(l) &= \begin{cases} x(l) & \text{if } l \in S \\ 0 & \text{otherwise.} \end{cases} \end{aligned}$$

⁴²⁴ Finally, given a vector or array $a \in \mathbb{R}^T$, we have the $l1$ normalization map

$$n: a \mapsto \frac{a}{\sum_{j=1}^T a_j}.$$

⁴²⁵ We define these objects as functions and functionals, but this is for notational convenience and
⁴²⁶ non-essential. A function $x(i) : \mathcal{B} \rightarrow [0, 1]$ is mathematically equivalent to the graph
⁴²⁷ $\mathcal{G}(x(i)) \in \mathcal{B} \times [0, 1]$. As an abuse of notation, we define $x \odot x' := z$ such that $z(l) = x(l)x'(l)$ for all $l \in \mathcal{B}$.
⁴²⁸ Also, denote $m(i)$ as the major structure containing experiment i . We then can write the
⁴²⁹ preprocessing algorithm.

PREPROCESS 1 Input Injection x , Projection y , Injection centroid $c \in \mathbb{R}^3$, Injection fraction F , data quality mask q

Injection fraction $x_F \leftarrow x \odot F$

Data-quality censor $y_q \leftarrow y \odot q$, $x_q \leftarrow x_F \odot q$

Restrict injection $x_m = 1|_m x_q$.

Compute centroid c from x_m

Regionalize $\tilde{y}_{\mathcal{T}} \leftarrow 1_{\mathcal{T}}(y_q)$

Normalize $y_{\mathcal{T}} \leftarrow n(\tilde{y}_{\mathcal{T}})$

Output $\tilde{y}_{\mathcal{T}}, c$

430 **Estimators**

431 As mentioned previously, we can consider our estimators as modeling a connectivity vector
 432 $f_{\mathcal{T}}(v, s) \in \mathbb{R}_{\geq 0}^T$. Thus, for the remainder of this section, we will discuss only $f(v, s)$. We review the
 433 Nadaraya-Watson estimator from ?, and describe its conversion into our cell-class specific Expected
 434 Loss estimator.

435 *Centroid-based Nadaraya-Watson* In the Nadaraya-Watson approach of ?, the injection is considered
 436 only through its centroid $c(i)$, and the projection is considered regionalized. That is,

$$f_*(i) = \{c(i), y_{\mathcal{T}}(i)\}.$$

437 Since the injection is considered only by its centroid, this model only generates predictions for
 438 particular locations l , and the prediction for a structure s is given by integrating over locations within
 439 the structure

$$f^*(\hat{f}(f_*(\mathcal{D})))(\nu, s) = \sum_{l \in s} \hat{f}(f_*(\mathcal{D}(I)))(\nu, l).$$

440 Here, I is the training data, and \hat{f} is the Nadaraya-Watson estimator

$$\hat{f}_{NW}(c(I), y_{\mathcal{T}}(I))(l) := \sum_{i \in I} \frac{\omega_{il}}{\sum_{i \in I} \omega_{il}} y_{\mathcal{T}}(i)$$

441 where $\omega_{il} := \exp(-\gamma d(l, c(i))^2)$ and d is the Euclidean distance between centroid $c(i)$ and voxel with
 442 position l .

443 Several facets of the estimator are visible here. A smaller γ corresponds to a greater amount of
 444 smoothing, and the index set $I \subseteq \{1 : n\}$ generally depends on s and ν . Varying γ bridges between
 445 1-nearest neighbor prediction and averaging of all experiments in I . In ?, I consisted of experiments
 446 sharing the same brain division, i.e. $I = I_m$, while restricting of index set to only include experiments
 447 with the same cell class gives the class-specific Cre-NW model. Despite this restriction, we fit γ by
 448 leave-one-out cross-validation for each m rather than a smaller subset like s or ν . That is,

$$\hat{\gamma}_m = \arg \min_{\gamma \in \mathbb{R}_{\geq 0}} \frac{1}{|\{s, \nu\}|} \sum_{s, \nu \in \{m, \mathcal{V}\}} \frac{1}{|I_s \cap I_\nu|} \sum_{i \in (I_s \cap I_\nu)} \ell(y_{\mathcal{T}}(i)), \hat{f}_{\mathcal{T}}(f_*(\mathcal{D}(\nu, s) \setminus i)). \quad (2)$$

⁴⁴⁹ *The Expected-Loss estimator* Besides location of the injection centroid, cell class also influences
⁴⁵⁰ projection. Thus, we introduce method for estimating the effect of Cre-distance, which we define as
⁴⁵¹ the distance between the projections of the mean experiment of one (Cre,leaf) pair with another. This
⁴⁵² method assigns a predictive weight to each pair of training points that depends both on their
⁴⁵³ centroid-distance and Cre-distance. This weight is determined by the expected prediction error of
⁴⁵⁴ each of the two feature types

⁴⁵⁵ We define Cre-line behavior as the average regionalized projection of a Cre-line in a given structure
⁴⁵⁶ (i.e. leaf). The vectorization of categorical information is known as **target encoding**

$$\bar{y}_{\mathcal{T},s,v} := \frac{1}{|I_s \cap I_v|} \sum_{i \in (I_s \cap I_v)} y_{\mathcal{T}}(i)$$

⁴⁵⁷ The Cre-distance is then defined a **Cre-distance** in a leaf to be the distance between the target-encoded
⁴⁵⁸ projections of two Cre-lines. The relative predictive accuracy of Cre-distance and centroid distance is
⁴⁵⁹ determined by fitting a surface of projection distance as a function of Cre-distance and centroid
⁴⁶⁰ distance.

⁴⁶¹ as determined by cross-validation. When we use shape-constrained B-splines to estimate this
⁴⁶² weight, the weights then may be said to be used in a Nadaraya-Watson estimator.

⁴⁶³ For this reason, we call this the Expected Loss Estimator. The resulting weights are then utilized in a
⁴⁶⁴ Nadaraya-Watson estimator in a final prediction step. increase the effective sample size of our
⁴⁶⁵ Nadaraya-Watson estimator,

⁴⁶⁶ In mathematical terms, our full feature set consists of the centroid coordinates and the
⁴⁶⁷ target-encoded means of the combinations of virus type and injection-centroid structure. That is,

$$f_*(\mathcal{D}_i) = \{c(i), \{\bar{y}_{\mathcal{T},s,v} \forall v\}, y_{\mathcal{T}}(i)\}.$$

⁴⁶⁸ f^* is defined as in (??). The expected loss estimator is then

$$\hat{f}_{EL}(c(I), y_{\mathcal{T}}(I))(l, v) := \sum_{i \in I} \frac{v_{ilv}}{\sum_{i \in I} v_{ilv}} y_{\mathcal{T}}(i)$$

⁴⁶⁹ where

$$v_{ilv} := \exp(-\gamma g(d(l, c(i))^2, d(\bar{y}_{\mathcal{T},s,v}, \bar{y}_{\mathcal{T},s,v(i)})^2))$$

⁴⁷⁰ and s is the structure containing l .

⁴⁷¹ The key step therefore is finding a suitable function g with which to weight the positional and Cre
⁴⁷² information. Note that g must be a concave, non-decreasing function of its arguments with with
⁴⁷³ $g(0, 0) = 0$. Then, g defines a metric on the product of the metric spaces defined by experiment
⁴⁷⁴ centroid and target-encoded cre-line, and \hat{f}_{EL} is a Nadaraya-Watson estimator. A derivation of this
⁴⁷⁵ fact is given later in this section.

⁴⁷⁶ therefore use shape-constrained B-splines to estimate g . In particular, B-splines is a method for
⁴⁷⁷ generating a predictive model

$$y =$$

⁴⁷⁸ In our setting, this gives us a surface the Cre-distance and centroid-distance to the
⁴⁷⁹ projection-distance response. Similarly to the Nadaraya-Watson model, we make the decision to fit a
⁴⁸⁰ g separately for each major brain division, and select \hat{g} as in [??](#). We compute our estimates using the
⁴⁸¹ pyGAM Python package [\(?\)](#).

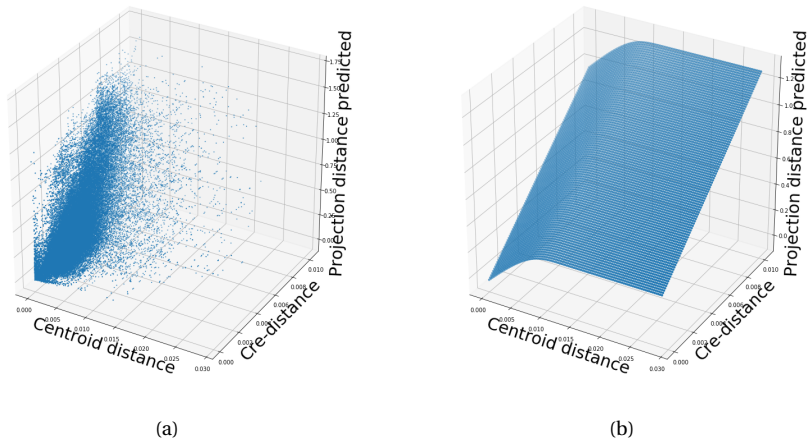


Figure 18: Fitting g . ?? Distribution of projection errors against centroid distance and cre-distance in Isocortex. ?? estimated \hat{g} using B-splines.

482 JUSTIFICATION OF SHAPE CONSTRAINT The shape-constrained expected-loss estimator introduced
 483 in this paper is, to our knowledge, novel. It should be considered an alternative method to the classic
 484 weighted kernel method. While we do not attempt a detailed theoretical study of this estimator, we do
 485 establish the need for the shape constraint in our spline estimator. Though this fact is probably well
 486 known, we prove a (slightly stronger) version here for completeness.

487 **Proposition 1.** *Given a collection of metric spaces X_1, \dots, X_n with metrics d_1, \dots, d_n (e.g. $d_{centroid}, d_{cre}$),
 488 and a function $f : (X_1 \times X_1) \dots \times (X_n \times X_n) = g(d_1(X_1 \times X_1), \dots, d_n(X_n \times X_n))$, then f is a metric if g is
 489 concave, non-decreasing and $g(d) = 0 \iff d = 0$.*

490 *Proof.* We show g satisfying the above properties implies that f is a metric.

- 491 ▪ The first property of a metric is that $f(x, x') = 0 \iff x = x'$. The left implication:
 492 $x = x' \implies f(x_1, x'_1, \dots, x_n, x'_n) = g(0, \dots, 0)$, since d are metrics. Then, since $g(0) = 0$, we have that
 493 $f(x, x') = 0$. The right implication: $f(x, x') = 0 \implies d = 0 \implies x = x'$ since d are metrics.
- 494 ▪ The second property of a metric is that $f(x, x') = f(x', x)$. This follows immediately from the
 495 symmetry of the d_i , i.e. $f(x, x') = f(x_1, x'_1, \dots, x_n, x'_n) = g(d_1(x_1, x'_1), \dots, d_n(x_n, x'_n)) =$
 496 $g(d_1(x'_1, x_1), \dots, d_n(x'_n, x_n)) = f(x'_1, x_1, \dots, x'_n, x_n) = f(x', x)$.
- 497 ▪ The third property of a metric is the triangle inequality: $f(x, x') \leq f(x, x^*) + f(x^*, x')$. To show this
 498 is satisfied for such a g , we first note that $f(x, x') = g(d(x, x')) \leq g(d(x, x^*) + d(x^*, x'))$ since g is
 499 non-decreasing and by the triangle inequality of d . Then, since g is concave,
 500 $g(d(x, x^*) + d(x^*, x')) \leq g(d(x, x^*)) + g(d(x^*, x')) = f(x, x^*) + f(x^*, x')$.

502 ***Setting a lower detection threshold***

503 The lower detection threshold of our approach is a complicated consequence of our experimental and
 504 analytical protocols. For example, the Nadaraya-Watson estimator is likely to generate many small
 505 false positive connections, since the projection of even a single experiment within the source region
 506 to a target will cause a non-zero connectivity in the Nadaraya-Watson weighted average. On the other
 507 hand, the complexities of the experimental protocol itself and the image analysis and alignment can
 508 also cause spurious signals. Therefore, it is of interest to establish a lower-detection threshold below
 509 which we have very little power-to-predict, and set estimated connectivities below this threshold to
 510 zero. This should make our estimated connectivities more accurate, especially in the
 511 biologically-important sense of sparsity.

512 We set this threshold with respect to the sum of Type 1 and Type 2 errors

$$\iota = \sum_{i \in \mathcal{E}} 1_{y_{\mathcal{T}}(i)=0}^T 1_{\hat{f}_{\mathcal{T}}(v(i), c(i)) > \tau} + 1_{y_{\mathcal{T}}(i) > 0}^T 1_{\hat{f}_{\mathcal{T}}(v(i), c(i)) < \tau}.$$

513 We then select the τ that minimizes ι . Results for this approach are given in Supplemental Section

514 ??.

515 ***Decomposing the connectivity matrix***

516 We utilize non-negative matrix factorization (NMF) to analyze the principal signals in our
 517 connectivity matrix. Here, we review this approach as applied to decomposition of the distal elements
 518 of the estimated connectivity matrix $\hat{\mathcal{C}}$ to identify q connectivity archetypes. Aside from the NMF
 519 program itself, the key elements are selection of the number of archetypes q and stabilization of the
 520 tendency of NMF to give random results over different initializations.

521 *Non-negative matrix factorization* As discussed in ?, one of the most basic processes underlying the
 522 observed connectivity is the tendency of each source region to predominantly project to proximal
 523 regions. For example, the heatmap in Supplemental Figure 17 shows that the pattern of intrastructure
 524 distances resembles the connectivity matrix in ?. These connections are biologically meaningful, but
 525 also unsurprising, and their relative strength biases learned latent coordinate representations away
 526 from long-range structures. For this reason, we establish a $1500\mu\text{m}$ 'distal' threshold within which to
 527 exclude connections for our analysis.

528 Given a matrix $X \in \mathbb{R}_{\geq 0}^{a \times b}$ and a desired latent space dimension q , the non-negative matrix
 529 factorization is thus

$$\text{NMF}(\mathcal{C}, \lambda, q, \mathbf{1}_M) = \arg \min_{W \in \mathbb{R}_{\geq 0}^{S \times q}, H \in \mathbb{R}_{\geq 0}^{q \times T}} \frac{1}{2} \|\mathbf{1}_M \odot \mathcal{C} - WH\|_2^2 + \lambda(\|H\|_1 + \|W\|_1).$$

530 The mask $\mathbf{1}_M$ specifies this objective for detecting patterns in long-range connections. We note the
 531 existence of NMF with alternative norms for certain marginal distributions, but leave utilization of
 532 this approach for future work (?).

533 The mask $\mathbf{1}_M \in \{0, 1\}^{S \times T}$ serves two purposes. First, it enables computation of the NMF objective
 534 while excluding self and nearby connections. These connections are both strong and linearly
 535 independent, and so would unduly influence the *NMF* reconstruction error over more biologically
 536 interesting or cell-type dependent long-range connections. Second, it enables cross-validation based
 537 selection of the number of retained components.

538 *Cross-validating NMF* We review cross-validation for NMF following (?). In summary, a NMF model is
 539 first fit on a reduced data set, and an evaluation set is held out. After random masking of the
 540 evaluation set, the loss of the learned model is then evaluated on the basis of successful
 541 reconstruction of the held-out values. This procedure is performed repeatedly, with replicates of
 542 random masks at each tested dimensionality q . This determines the point past which additional
 543 hidden units provide no additional value for reconstructing the original signal.

544 The differentiating feature of cross-validation for NMF compared with supervised learning is the
 545 randomness of the masking matrix 1_M . Cross-validation for supervised learning generally leaves out
 546 entire observations, but this is insufficient for our situation. This is because, given W , our H is the
 547 solution of a regularized non-negative least squares optimization problem

$$H := \hat{e}_W(1_M \odot \mathcal{C}) = \arg \min_{\beta \in \mathbb{R}_{\geq 0}^{q \times T}} \|1_M \odot \mathcal{C} - W\beta\|_2^2 + \|\beta\|_1. \quad (3)$$

548 The negative effects of an overfit model can therefore be optimized away from on the evaluation set.

A standard solution is to generate uniformly random masks $1_{M(p)} \in \mathbb{R}^{S \times T}$ where

$$1_{M(p)}(s, t) \sim \text{Bernoulli}(p).$$

NMF is then performed using the mask $1_{M(p)}$ to get W . The cross-validation error is then

$$\epsilon_q = \frac{1}{R} \sum_{r=1}^R (\|1_{M(p)_r^c} \odot X - W(\hat{e}_W(1_{M(p)_r^c} \odot X))\|_2^2$$

where $1_{M(p)_r}^c$ is the binary complement of $1_{M(p)_r}$ and R is a number of replicates. Theoretically, the optimum number of components is then

$$\hat{q} = \operatorname{arg\,min}_q \epsilon_q.$$

549 *Stabilizing NMF* The NMF program is non-convex, and, empirically, individual replicates will not
 550 converge to the same optima. One solution therefore is to run multiple replicates of the NMF
 551 algorithm and cluster the resulting vectors. This approach raises the questions of how many clusters
 552 to use, and how to deal with stochasticity in the clustering algorithm itself. We address this issue
 553 through the notion of clustering stability (?).

The clustering stability approach is to generate L replicas of k-cluster partitions $\{C_{kl} : l \in 1 \dots L\}$ and then compute the average dissimilarity between clusterings

$$\xi_k = \frac{2}{L(L-1)} \sum_{l=1}^L \sum_{l'=1}^l d(C_{kl}, C_{kl'}).$$

Then, the optimum number of clusters is

$$\hat{k} = \arg \min_k \xi_k.$$

554 A review of this approach is found in ?. Intuitively, archetype vectors that cluster together frequently
 555 over clustering replicates indicate the presence of a stable clustering. For d , we utilize the adjusted
 556 Rand Index - a simple dissimilarity measure between clusterings. Note that we expect to select slightly
 557 more than the q components suggested by cross-validation, since archetype vectors which appear in
 558 one NMF replicate generally should appear in others. We then select the q clusters with the most
 559 archetype vectors - the most stable NMF results - and take the median of each cluster to create a
 560 sparse representative archetype ?. We then find the according H using Program ?. Experimental
 561 results for these cross-validation and stability selection approaches are given in Supplemental Section
 562 ??.

7 SUPPLEMENTAL EXPERIMENTS

563 Setting detection threshold τ

564 We give results on the false detection rate at different limits of detection. These conclusively show that
 565 10^{-6} is the good threshold for our normalized data.

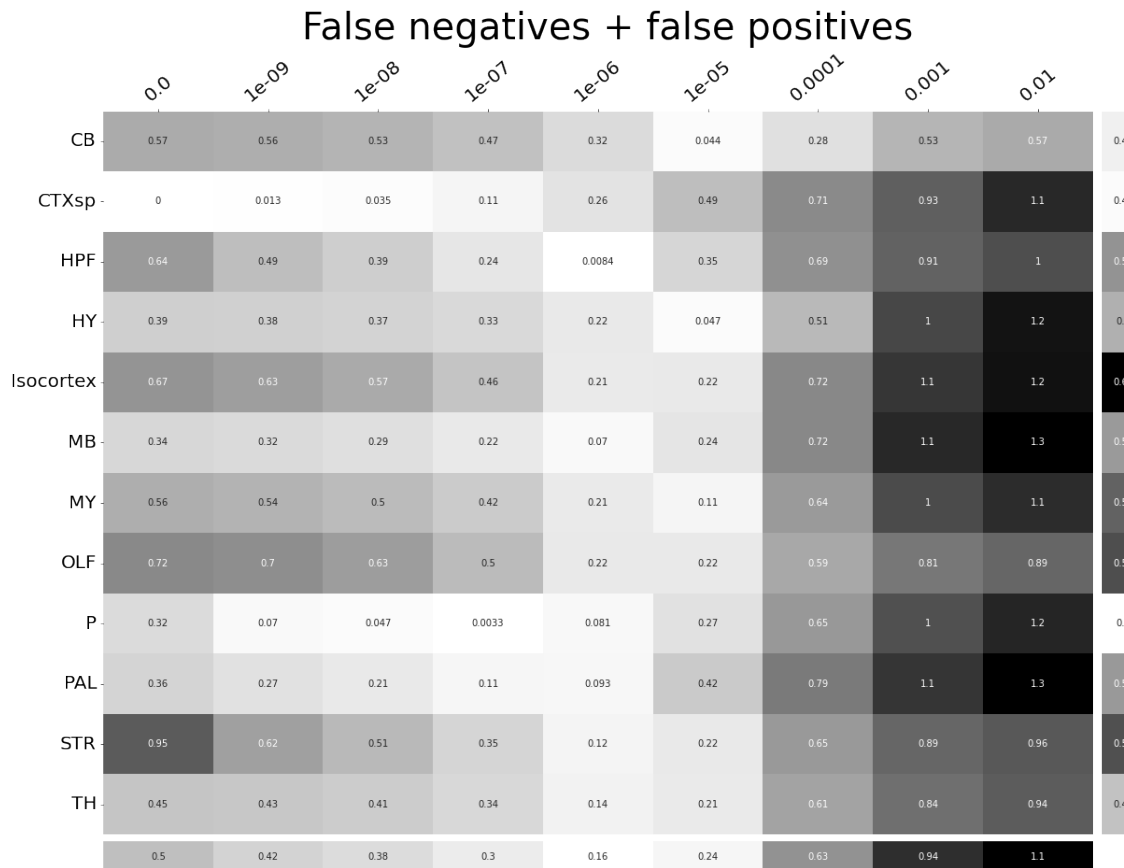


Figure 19: τ at different limits of detection in different major structures. 10^{-6} is the optimal detection threshold.

566 ***Loss subsets***

567 We report model accuracies for our *EL* model by neuron class and structure. These expand upon the
 568 results in Table 2 and give more specific information about the quality of our estimates. CTXsp is
 569 omitted due to the small nature of the evaluation set.

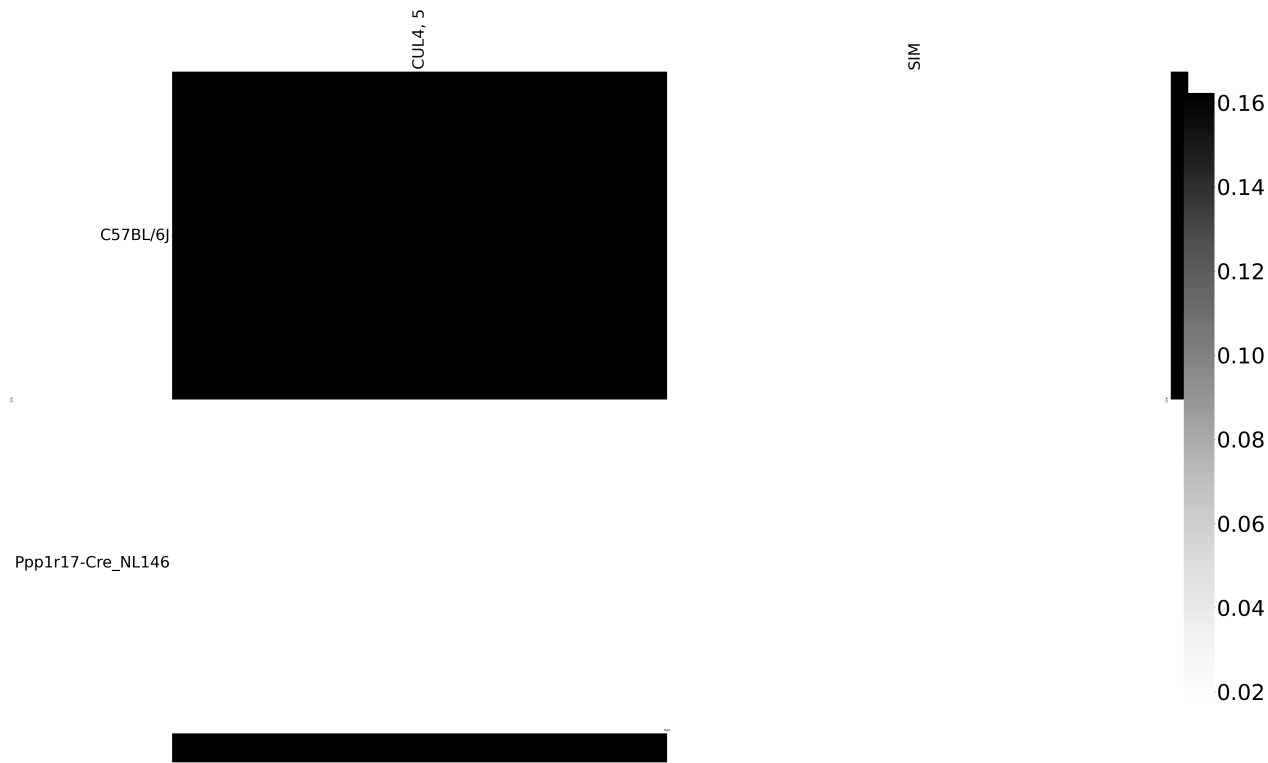


Figure 20: Weighted loss for cre-leaf combinations in CB. Missing values are omitted. Row and column averages are also plotted.

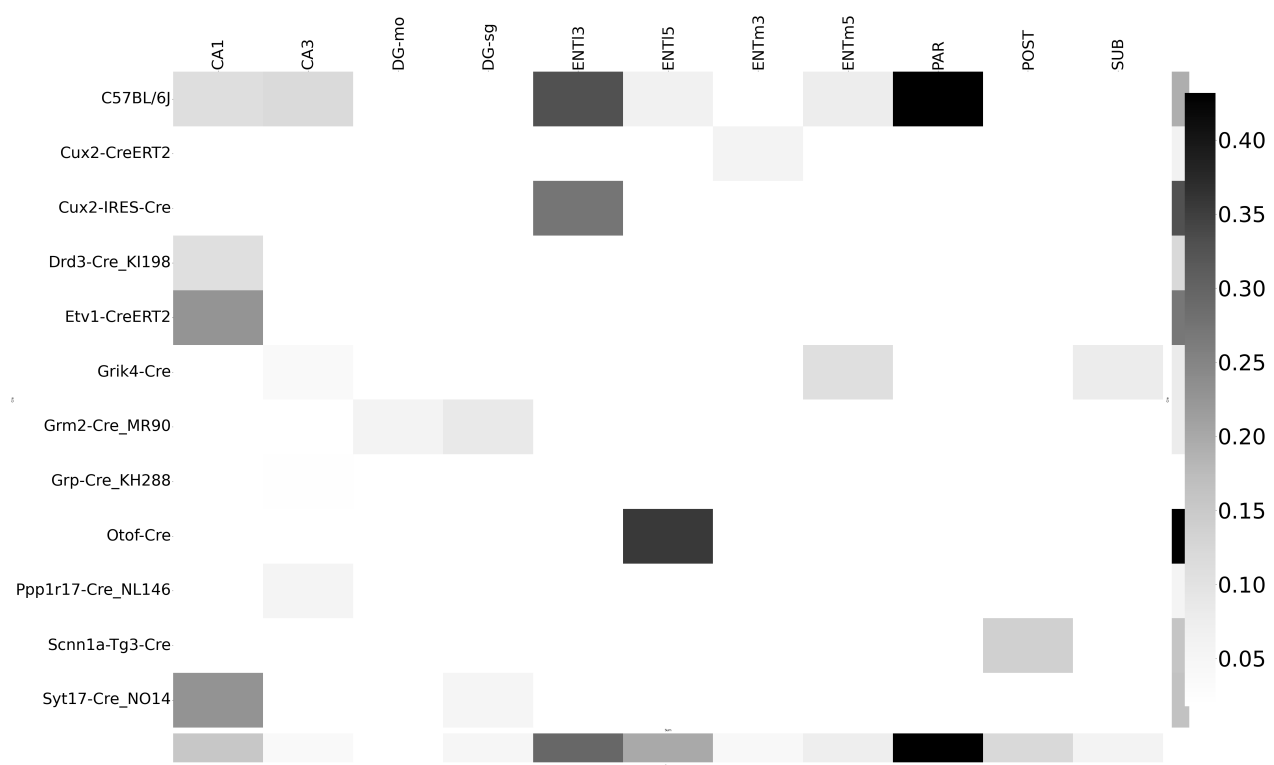


Figure 21: Weighted loss for cre-leaf combinations in HPF. Missing values are omitted. Row and column averages are also plotted.

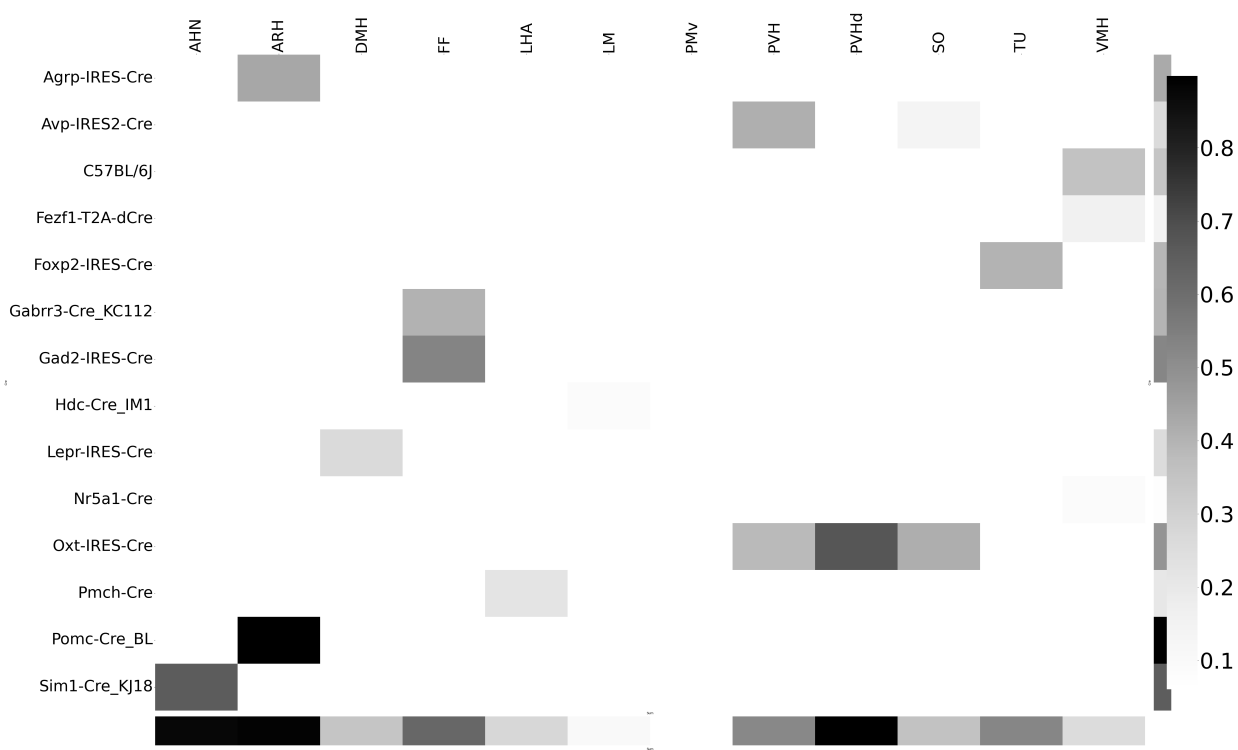


Figure 22: Weighted loss for cre-leaf combinations in HY. Missing values are omitted. Row and column averages are also plotted.

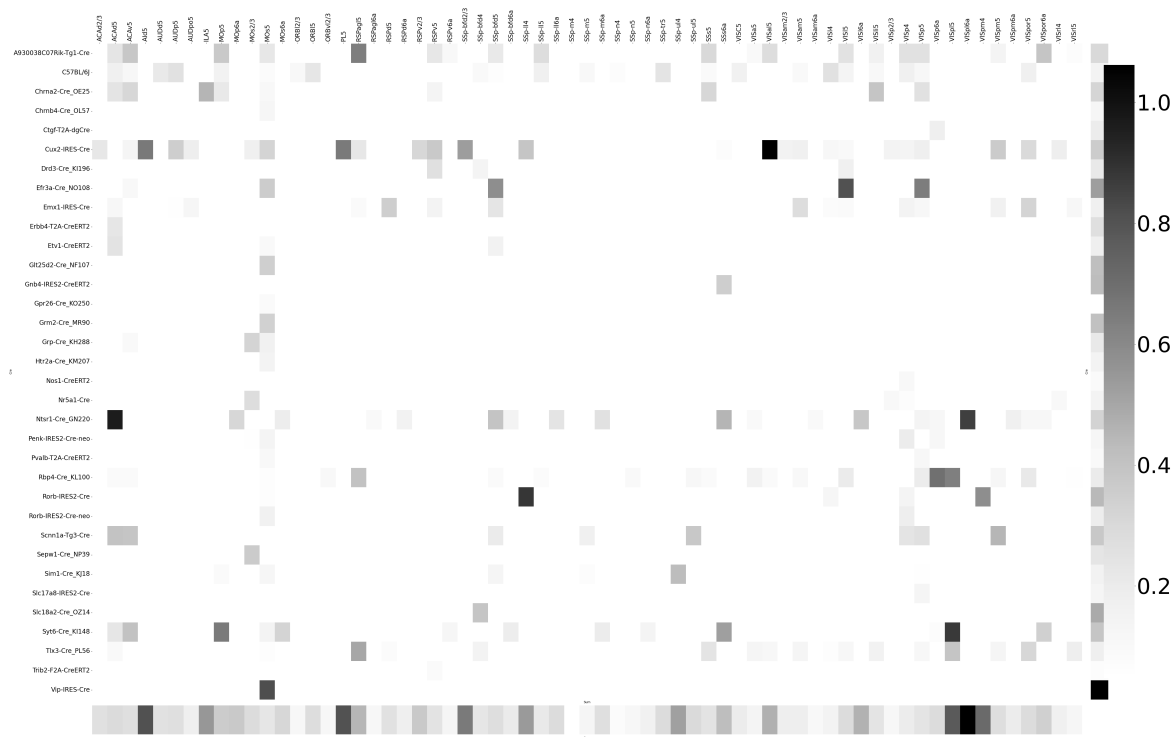


Figure 23: Weighted loss for cre-leaf combinations in Isocortex. Missing values are omitted. Row and column averages are also plotted.

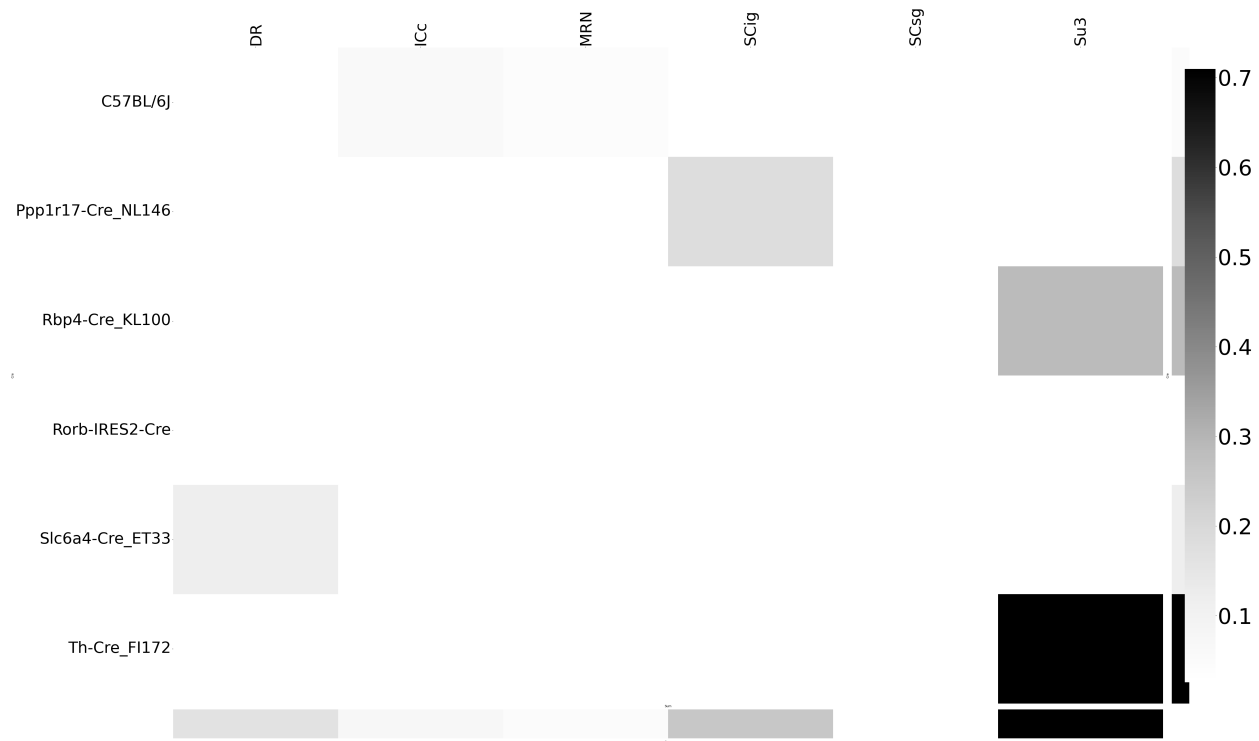


Figure 24: Weighted loss for cre-leaf combinations in MB. Missing values are omitted. Row and column averages are also plotted.

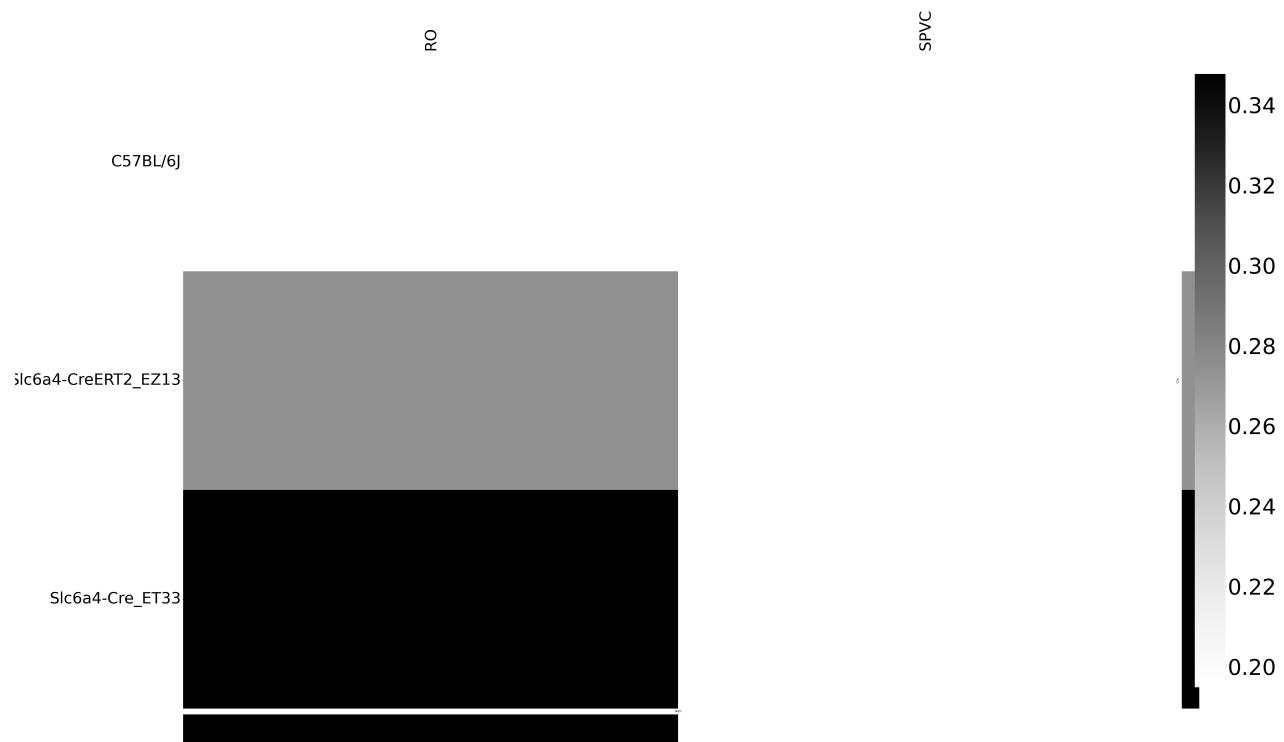


Figure 25: Weighted loss for cre-leaf combinations in MY. Missing values are omitted. Row and column averages are also plotted.

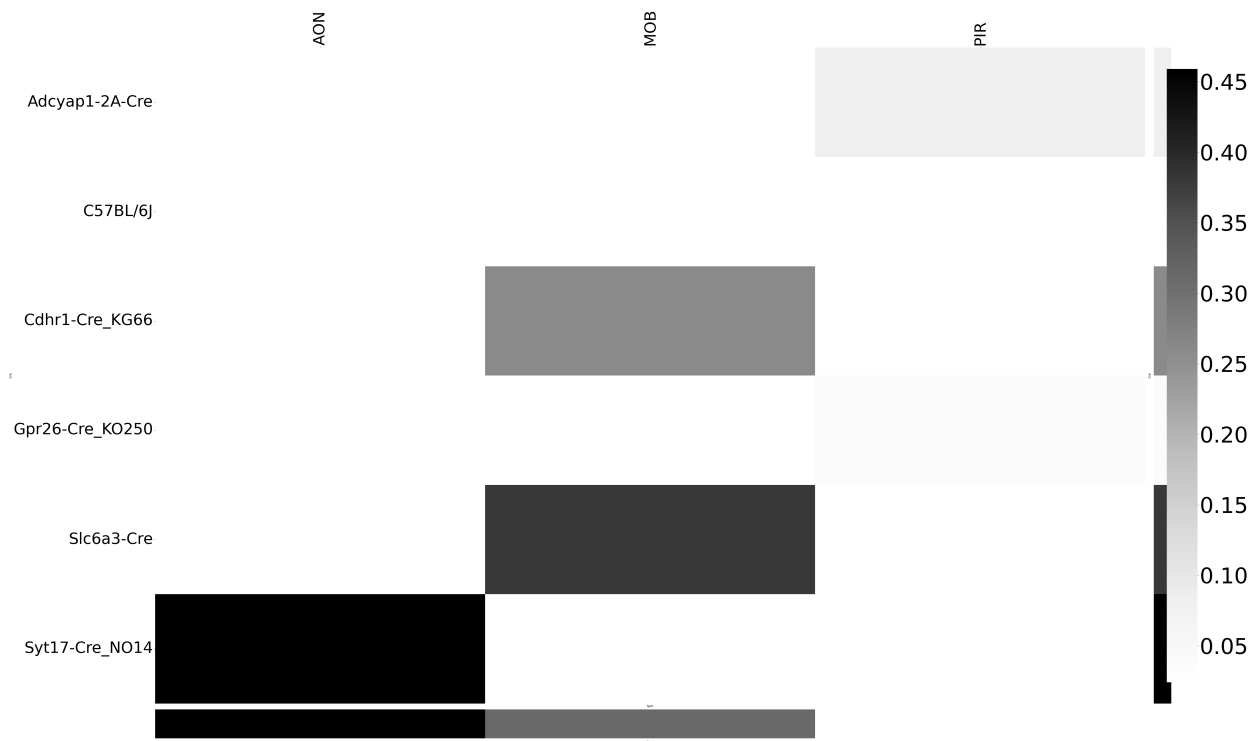


Figure 26: Weighted loss for cre-leaf combinations in OLF. Missing values are omitted. Row and column averages are also plotted.

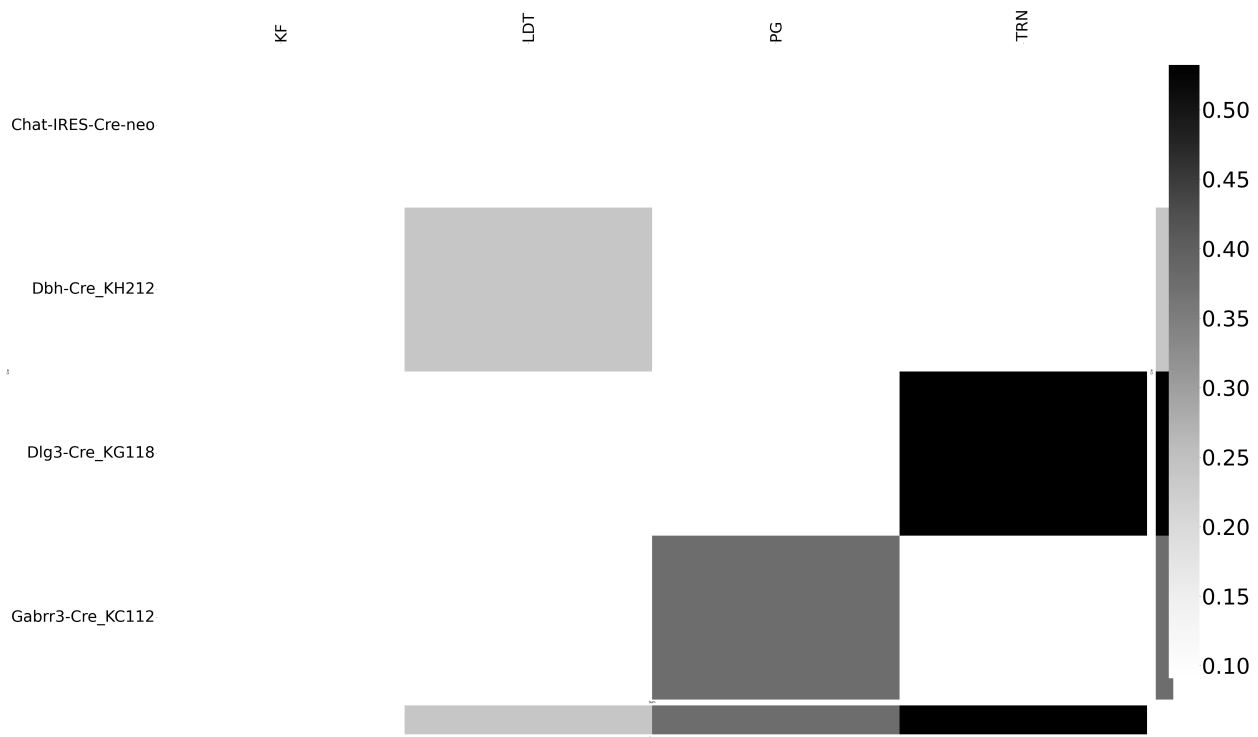


Figure 27: Weighted loss for cre-leaf combinations in P. Missing values are omitted. Row and column averages are also plotted.

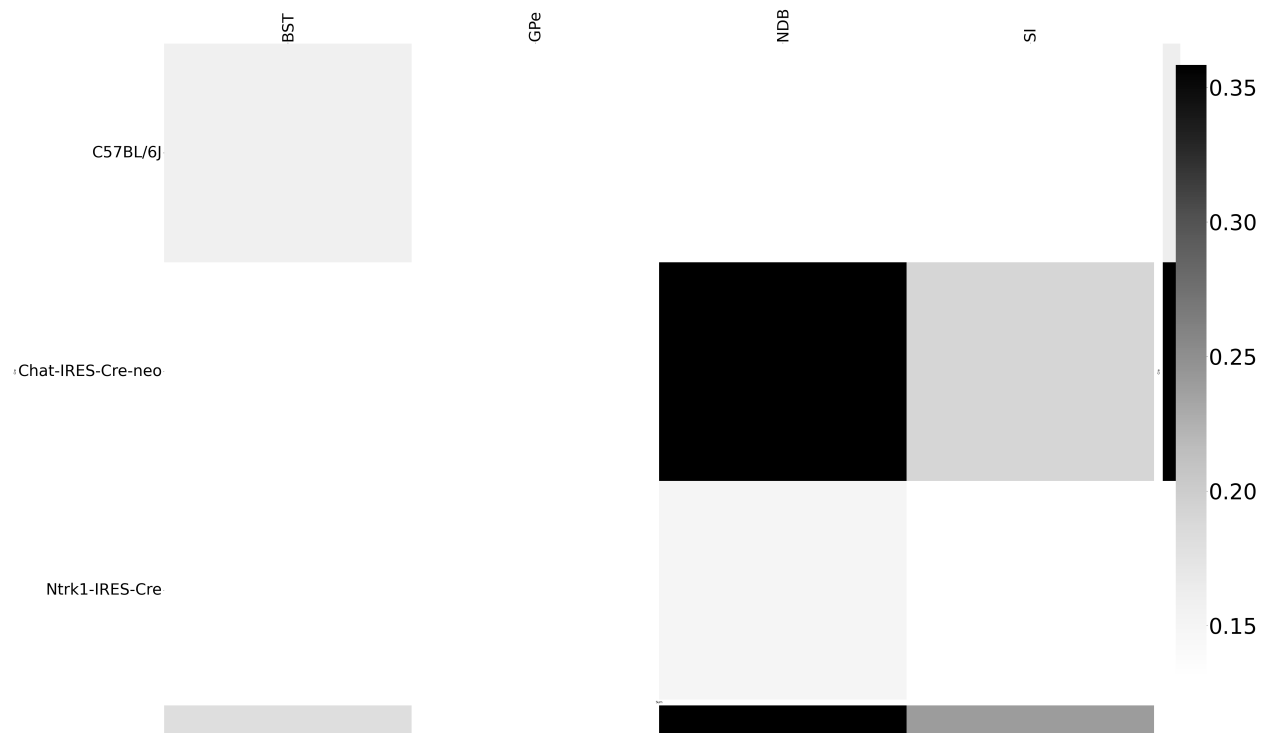


Figure 28: Weighted loss for cre-leaf combinations in PAL. Missing values are omitted. Row and column averages are also plotted.

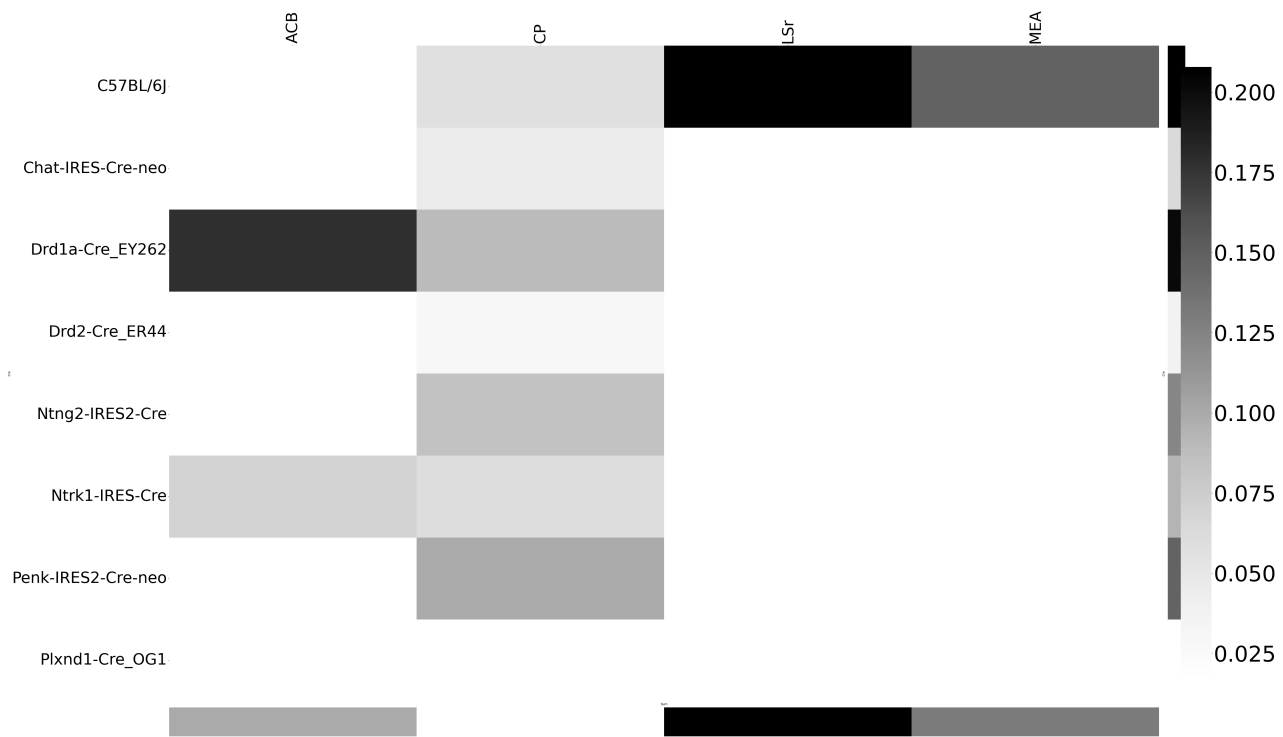


Figure 29: Weighted loss for cre-leaf combinations in STR. Missing values are omitted. Row and column averages are also plotted.

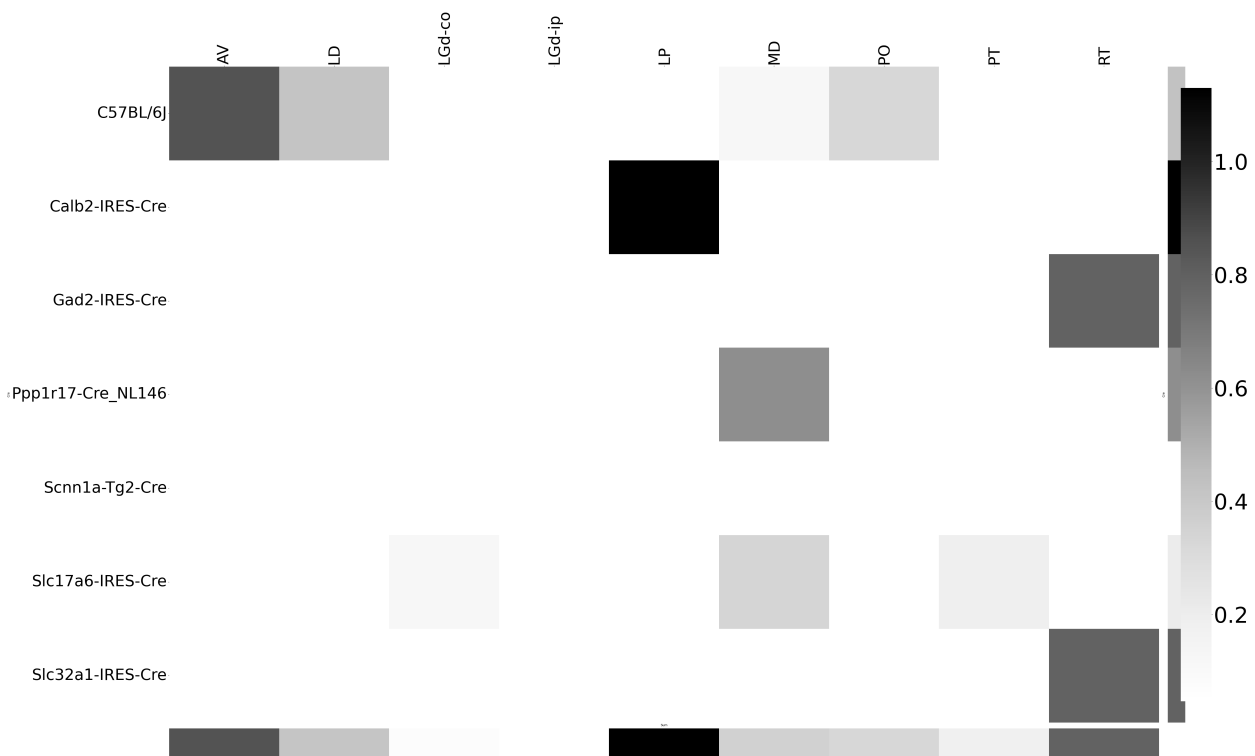


Figure 30: Weighted loss for cre-leaf combinations in TH. Missing values are omitted. Row and column averages are also plotted.

570 **Matrix Factorization**

571 We give additional results on the generation of the archetypal connectome patterns. These consist of
 572 cross-validation selection of q , the number of latent components, stability analysis, and visualization
 573 of the reconstructed wild-type connectivity.

574 *Cross-validation* We set $\alpha = 0.002$ and run Program 2 on \mathcal{C}_{wt} . We use a random mask with $p = .3$ to
 575 evaluate prediction accuracy of models trained on the unmasked data on the masked data. To
 576 account for stochasticity in the NMF algorithm, we run $R = 8$ replicates at each potential dimension q .
 577 This selects $\hat{q} = 60$.

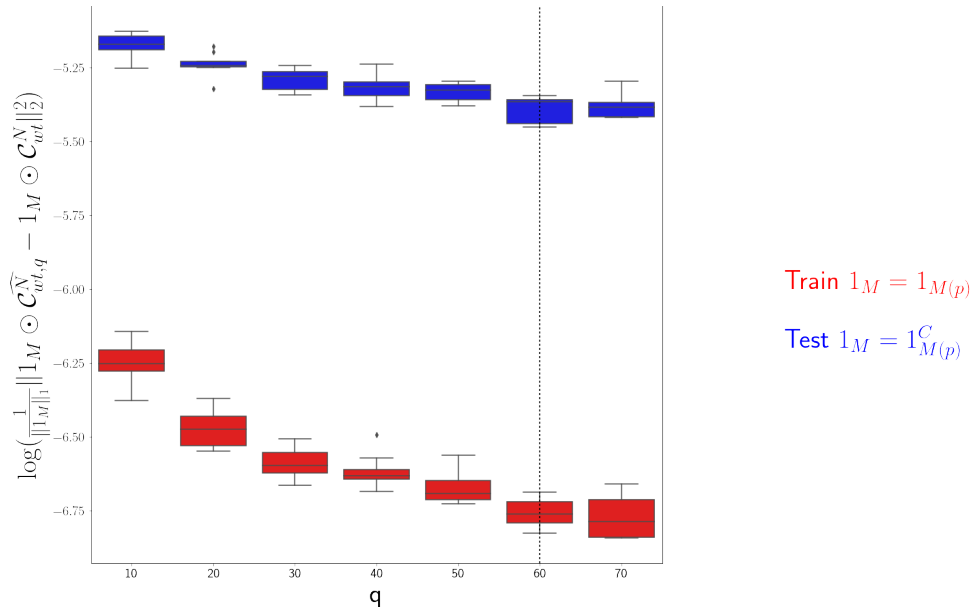


Figure 31: Train and test error using NMF decomposition.

578 *Stability* For the purposes of visualization and interpretability, we restrict to a $q = 15$ component
 579 model. To address the instability of the NMF algorithm in identifying components, we $k - means$
 580 cluster components over $R = 10$ replicates with $k \in \{10, 15, 20, 25, 30\}$. Since the clustering is itself
 581 unstable, we repeat the clustering 25 times and select the k with the largest Rand index.

582 q	10.000000	20.000000	30.000000	40.000000	50.000000
Rand index	0.772544	0.844981	0.932957	0.929827	0.885862

583 Since k -means is most stable at $k = 30$, we cluster the $qR = 150$ components into 30 clusters and
 584 select the 15 clusters appearing in the most replicates.

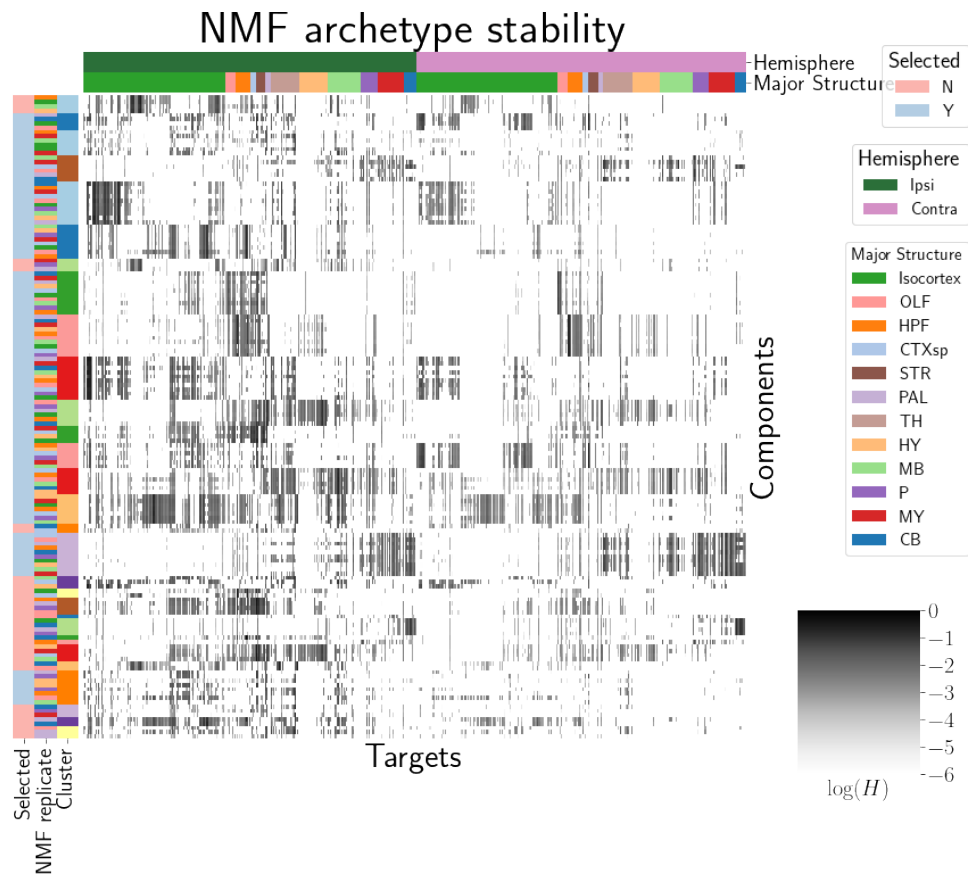


Figure 32: Stability of NMF results across replicates. Replicate and NMF component are shown on rows. Components that are in the top 15 are also indicated.

585 These are the components whose medians are plotted in Figure 4a.

8 COMPETING INTERESTS

586 This is an optional section. If you declared a conflict of interest when you submitted your manuscript,
587 please use this space to provide details about this conflict.

588

589

590

REFERENCES

- 591 Brunet, J.-P., Tamayo, P., Golub, T. R., & Mesirov, J. P. (2004). Metagenes and molecular pattern discovery using matrix
592 factorization. *Proc. Natl. Acad. Sci. U. S. A.*, 101(12), 4164–4169.
- 593 Chamberlin, N. L., Du, B., de Lacalle, S., & Saper, C. B. (1998). Recombinant adeno-associated virus vector: use for
594 transgene expression and anterograde tract tracing in the CNS. *Brain Res.*, 793(1-2), 169–175.
- 595 Daigle, T. L., Madisen, L., Hage, T. A., Valley, M. T., Knoblich, U., Larsen, R. S., ... Zeng, H. (2018). A suite of transgenic
596 driver and reporter mouse lines with enhanced Brain-Cell-Type targeting and functionality. *Cell*, 174(2), 465–480.e22.
- 597 Gao, Y., Zhang, X., Wang, S., & Zou, G. (2016). Model averaging based on leave-subject-out cross-validation. *J. Econom.*,
598 192(1), 139–151.
- 599 Harris, J. A., Mihalas, S., Hirokawa, K. E., Whitesell, J. D., Choi, H., Bernard, A., ... Zeng, H. (2019). Hierarchical
600 organization of cortical and thalamic connectivity. *Nature*, 575(7781), 195–202.
- 601 Harris, J. A., Oh, S. W., & Zeng, H. (2012). Adeno-associated viral vectors for anterograde axonal tracing with fluorescent
602 proteins in nontransgenic and cre driver mice. *Curr. Protoc. Neurosci., Chapter 1, Unit 1.20.1–18*.
- 603 Harris, K. D., Mihalas, S., & Shea-Brown, E. (2016). Nonnegative spline regression of incomplete tracing data reveals high
604 resolution neural connectivity.
- 605 Huang, K. W., Ochandarena, N. E., Philson, A. C., Hyun, M., Birnbaum, J. E., Cicconet, M., & Sabatini, B. L. (2019).
606 Molecular and anatomical organization of the dorsal raphe nucleus. *Elife*, 8.
- 607 Jeong, M., Kim, Y., Kim, J., Ferrante, D. D., Mitra, P. P., Osten, P., & Kim, D. (2016). Comparative three-dimensional
608 connectome map of motor cortical projections in the mouse brain. *Sci. Rep.*, 6, 20072.
- 609 Knox, J. E., Harris, K. D., Graddis, N., Whitesell, J. D., Zeng, H., Harris, J. A., ... Mihalas, S. (2019). High-resolution
610 data-driven model of the mouse connectome. *Netw Neurosci*, 3(1), 217–236.
- 611 Kotliar, D., Veres, A., Nagy, M. A., Tabrizi, S., Hodis, E., Melton, D. A., & Sabeti, P. C. (2019). Identifying gene expression
612 programs of cell-type identity and cellular activity with single-cell RNA-Seq. *Elife*, 8.

- 613 Li, X., Yu, B., Sun, Q., Zhang, Y., Ren, M., Zhang, X., ... Qiu, Z. (2018). Generation of a whole-brain atlas for the
 614 cholinergic system and mesoscopic projectome analysis of basal forebrain cholinergic neurons. *Proc. Natl. Acad. Sci.*
 615 *U. S. A.*, 115(2), 415–420.
- 616 Lotfollahi, M., Naghipourfar, M., Theis, F. J., & Alexander Wolf, F. (2019). Conditional out-of-sample generation for
 617 unpaired data using trVAE.
- 618 Muzerelle, A., Scotto-Lomassese, S., Bernard, J. F., Soiza-Reilly, M., & Gaspar, P. (2016). Conditional anterograde tracing
 619 reveals distinct targeting of individual serotonin cell groups (B5-B9) to the forebrain and brainstem. *Brain Struct.*
 620 *Funct.*, 221(1), 535–561.
- 621 Oh, S. W., Harris, J. A., Ng, L., Winslow, B., Cain, N., Mihalas, S., ... Zeng, H. (2014). A mesoscale connectome of the
 622 mouse brain. *Nature*, 508(7495), 207–214.
- 623 Ren, J., Friedmann, D., Xiong, J., Liu, C. D., Ferguson, B. R., Weerakkody, T., ... Luo, L. (2018). Anatomically defined and
 624 functionally distinct dorsal raphe serotonin sub-systems. *Cell*, 175(2), 472–487.e20.
- 625 Ren, J., Isakova, A., Friedmann, D., Zeng, J., Grutzner, S. M., Pun, A., ... Luo, L. (2019). Single-cell transcriptomes and
 626 whole-brain projections of serotonin neurons in the mouse dorsal and median raphe nuclei. *Elife*, 8.
- 627 Saul, L. K., & Roweis, S. T. (2003). Think globally, fit locally: Unsupervised learning of low dimensional manifolds. *J.*
 628 *Mach. Learn. Res.*, 4(Jun), 119–155.
- 629 Servén D., B. C. (n.d.). *pygam: Generalized additive models in python*.
- 630 von Luxburg, U. (2010a). Clustering stability: An overview.
- 631 von Luxburg, U. (2010b). Clustering stability: An overview.
- 632 Watson, C., Paxinos, G., & Puelles, L. (2012). The mouse nervous system..
- 633 Wu, S., Joseph, A., Hammonds, A. S., Celiker, S. E., Yu, B., & Frise, E. (2016). Stability-driven nonnegative matrix
 634 factorization to interpret spatial gene expression and build local gene networks. *Proc. Natl. Acad. Sci. U. S. A.*, 113(16),
 635 4290–4295.
- 636 Zaborszky, L., Csordas, A., Mosca, K., Kim, J., Gielow, M. R., Vadasz, C., & Nadasdy, Z. (2015). Neurons in the basal
 637 forebrain project to the cortex in a complex topographic organization that reflects corticocortical connectivity

638 patterns: an experimental study based on retrograde tracing and 3D reconstruction. *Cereb. Cortex*, 25(1), 118–137.

9 TECHNICAL TERMS

639 **Technical Term** a key term that is mentioned in an NETN article and whose usage and definition may
640 not be familiar across the broad readership of the journal.

641 **Cre-line** Refers to the combination of cre-recombinase expression in transgenic mouse and
642 cre-induced promotion in the vector that induces labelling of cell-class specific projection.

643 **Cell class** The projecting neurons targeted by a particular cre-line

644 **Structural connectivities** connectivity between structures

645 **Voxel** A $100\mu m$ cube of brain.

646 **Structural connection tensor** Connectivities between structures given a neuron class

647 **dictionary-learning** A family of algorithms for finding low-dimensional data representations.

648 **Shape constrained estimator** A statistical estimator that fits a function of a particular shape (e.g.
649 monotonic increasing, convex).

650 **Nadaraya-Watson** A simple smoothing estimator.

651 **Connectivity archetypes** Typical connectivity patterns

652 **Expected loss** Our new estimator that weights different features by their estimated predictive
653 power.